Drgania w konstrukcjach lotniczych

Przegląd metod przewidywania drgań w środowisku powietrznym

Prognozowanie środowiska reakcji na drgania samolotu, które jest przyjmowane we wstępnym opracowywaniu samolotów, nie było jeszcze wystarczająco rozwiązane i nie znalazło szerokiego zastosowania. W tym wykładzie , po pierwsze, krótko omówiono teoretyczne i inżynieryjne znaczenie przewidywania warunków reakcji na drgania samolotu. Następnie podsumowujemy główne metody przewidywania odpowiedzi drgań samolotu oraz wskażemy na ich zalety, wady i zakresy zastosowania, w tym ekstrapolację podobnej struktury, analizę teoretyczną i rozwiązanie analityczne różniczkowego równania dynamicznego, modelowanie parametrów statystycznych, modelowanie obliczeń symulacyjnych i uczenie maszynowe.

Ground Vibration and Flight Flutter Tests of the Single-Seat F-16XL Aircraft With a Modified Wing

The NASA single-seat F-16XL aircraft was modified by the addition of a glove to the left wing. Vibration tests were conducted on the ground to assess the changes to the aircraft caused by the glove. Flight flutter testing was conducted on the aircraft with the glove installed to ensure that the flight envelope was free of aeroelastic or aeroservoelastic instabilities. The ground vibration tests showed that above 20 Hz, several modes that involved the control surfaces were significantly changed. Flight test data showed that modal damping levels and trends were satisfactory where obtainable. The data presented in this report include estimated modal parameters from the ground vibration and flight flutter test.

Jednomiejscowy samolot został zmodyfikowany przez dodanie rękawicy do skrzydła. Test wibracyjny przeprowadzono na ziemi, aby ocenić zmiany, jakie zachodzą w samolocie na lewym skrzydle. Na samolocie z instalacją rękawicową przeprowadzono testy trzepotania lotu, aby upewnić się, że charakterystyka lotu jest wolna od niestabilności aerosprężystej. Testy wibracji na ziemi wykazały, że powyżej 20 Hz kilka modów, które obejmowały powierzchnie sterowe, było znacznie słabszych. Dane z testów w locie wykazały, że poziomy i trendy tłumienia modalnego były zadowalające.

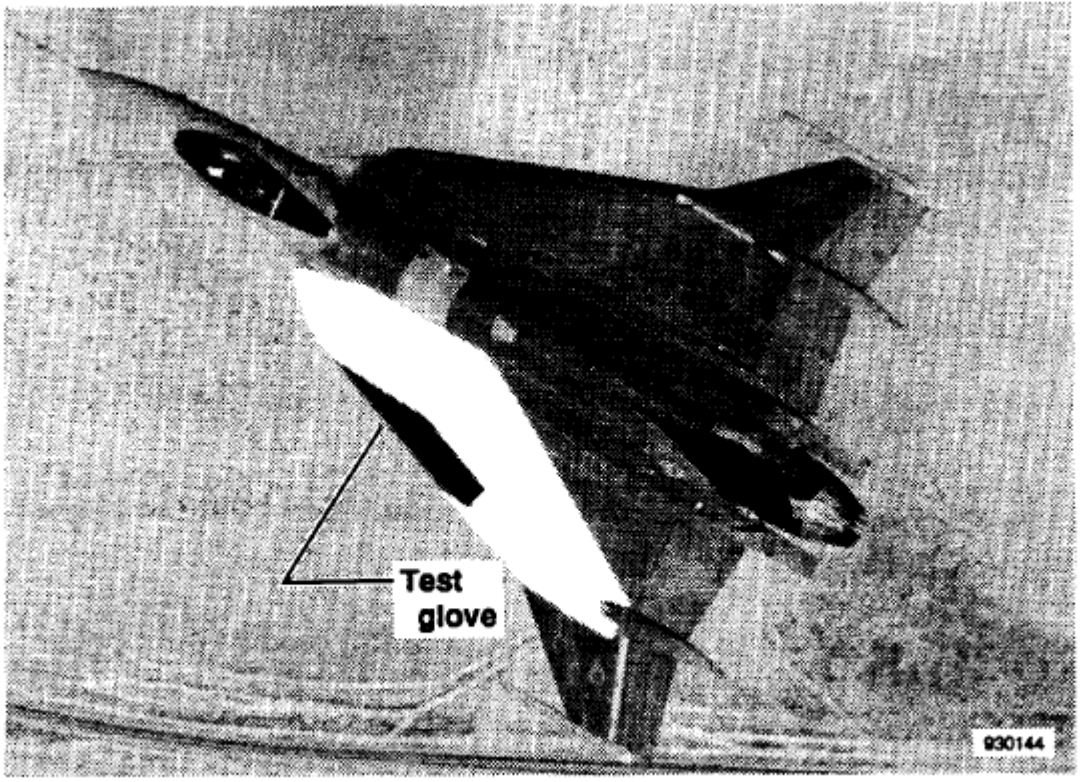

Figure 1. NASA F-16XL single-seat aircraft with the test glove installed on the left wing.

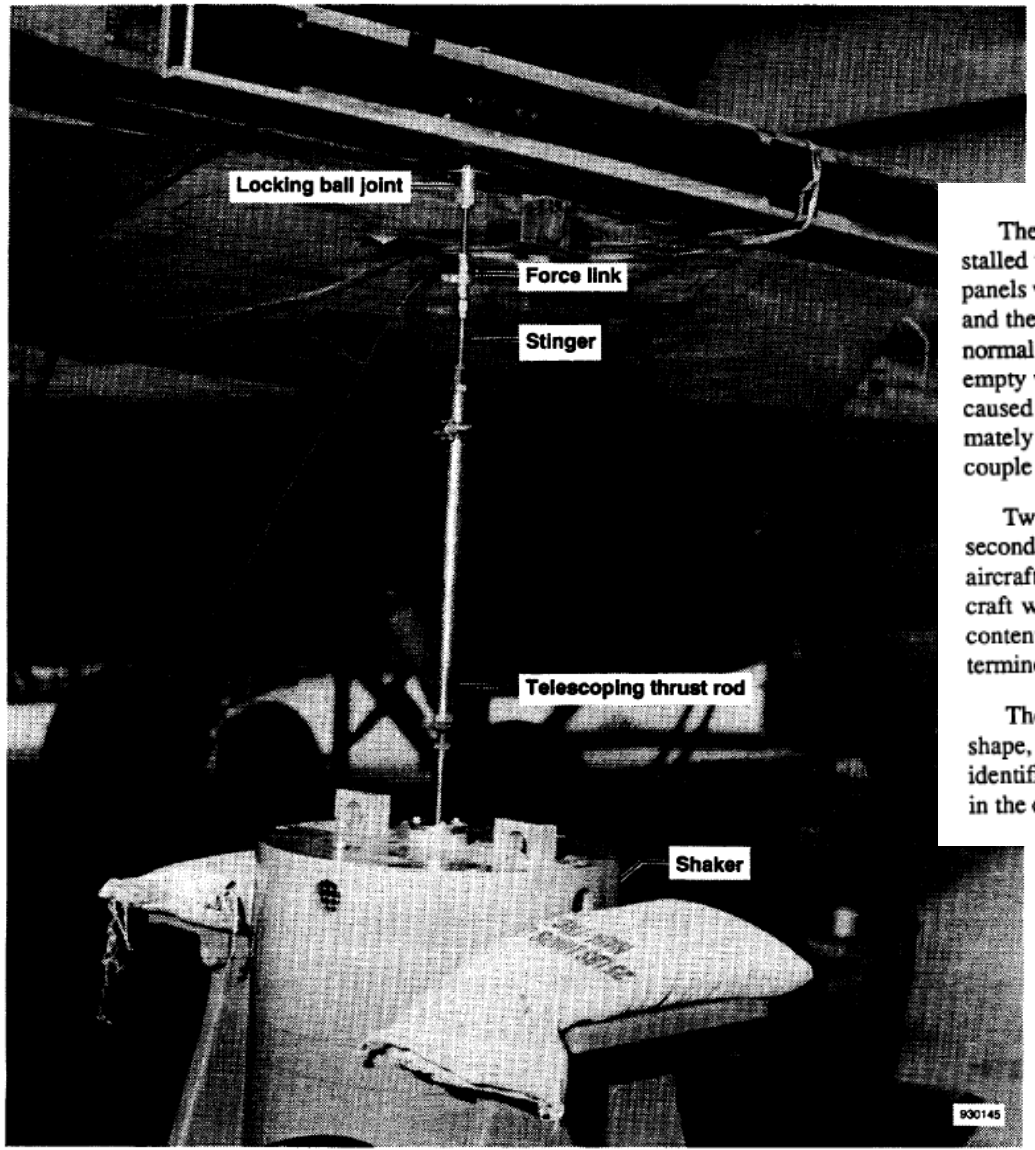

Figure 5. GVT excitation shaker setup.

The GVTs were conducted on an essentially flight-ready aircraft. Some equipment that was not yet installed was simulated by ballast weights placed as close to the proper locations as possible. All structural panels were fastened and the canopy closed and locked. The aircraft was on its landing gear during the test and the struts were collapsed to eliminate potential nonlinearities. The tires were deflated to one-half the normal pressure to provide a softer support. Fuel loading for both tests consisted of full fuselage tanks and empty wing tanks. The control surfaces were in the trim position for each test and potential nonlinearities caused by excessive actuator freeplay in the elevons and ailerons was minimized by suspending approximately 50 lb of lead shot from the surfaces with an elastic bungee cord. The bungee cord was used to decouple the dynamics of the lead shot from the aircraft.

Two GVTs were performed on the aircraft—one before the glove installation (baseline GVT) and a second after (modified GVT). The general procedure for each GVT was to install accelerometers on the aircraft and then connect them to a digital data-acquisition system with some signal conditioning. The aircraft was excited by three electrodynamic shakers using uncorrelated random signals with a frequency content of 1 to 50 Hz. Frequency response functions (FRFs) were estimated and subsequently used to determine the structural frequencies and mode shapes below 30 Hz.

The data were analyzed by estimating the aircraft's modal parameters of frequency, damping, and mode shape, and then by comparing the baseline and modified GVT results for significant modal changes. The identification of the modal frequencies was simplified by using all 540 FRFs (3 inputs and 180 responses) in the calculation of the multivariate mode indicator functions (MMIFs) for each configuration.

Flight Test

The flight-flutter clearance was accomplished by obtaining test data at 14 test points (fig. 7) flown in order of increasing dynamic pressure over a series of three flights. At each test point, data were obtained during 60 sec of stabilized flight. Atmospheric turbulence provided structural excitation. Because of the lack of turbulence at some test points, a series of pilot-induced control surface pulses supplemented the turbulence excitation. The accelerometer responses were monitored in real time for any aircraft instabilities and were used for near-real-time modal frequency and damping calculations. These results were then evaluated before clearing the aircraft to the next test point.

Near-real-time and postflight data analysis consisted of calculating the autopower spectra. Then a frequency range of interest was identified and the rest of the spectrum was set to zero. The inversed Fourier-transformed was performed on the spectrum and an exponential window was applied. Transformation back to the frequency domain resulted in a smoothed spectrum from which a half-power method was used to estimate the structural frequency and damping (ref. 13).

Because the time available for data analysis was restricted during flight, the data were more thoroughly analyzed between flights using the same reduction techniques. Postflight analysis established confidence levels in estimated modal frequency and damping values by providing more estimates and using statistical averages and variances on the results. It also provided the opportunity for further manipulation of the data, such as addition and subtraction of wingtip sensor data to enhance symmetric and antisymmetric motion, which also aided in separating closely spaced modes.

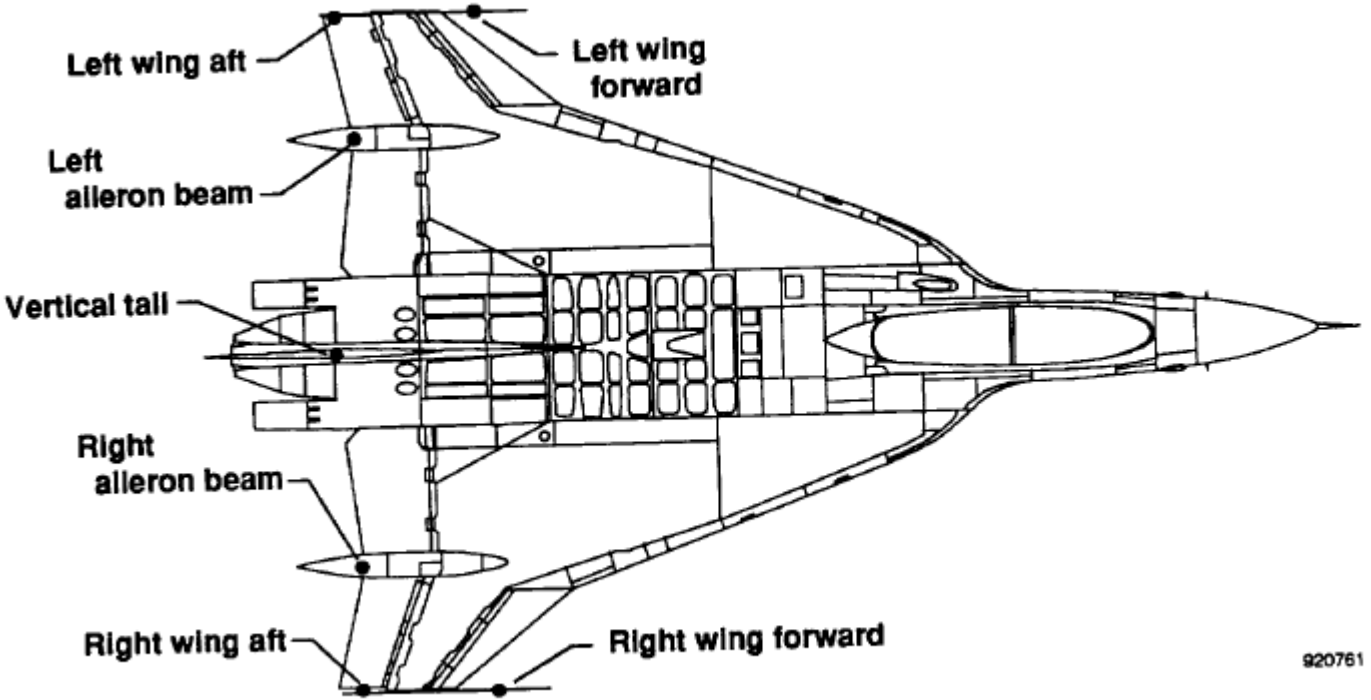

Figure 6. Flight test accelerometer locations.

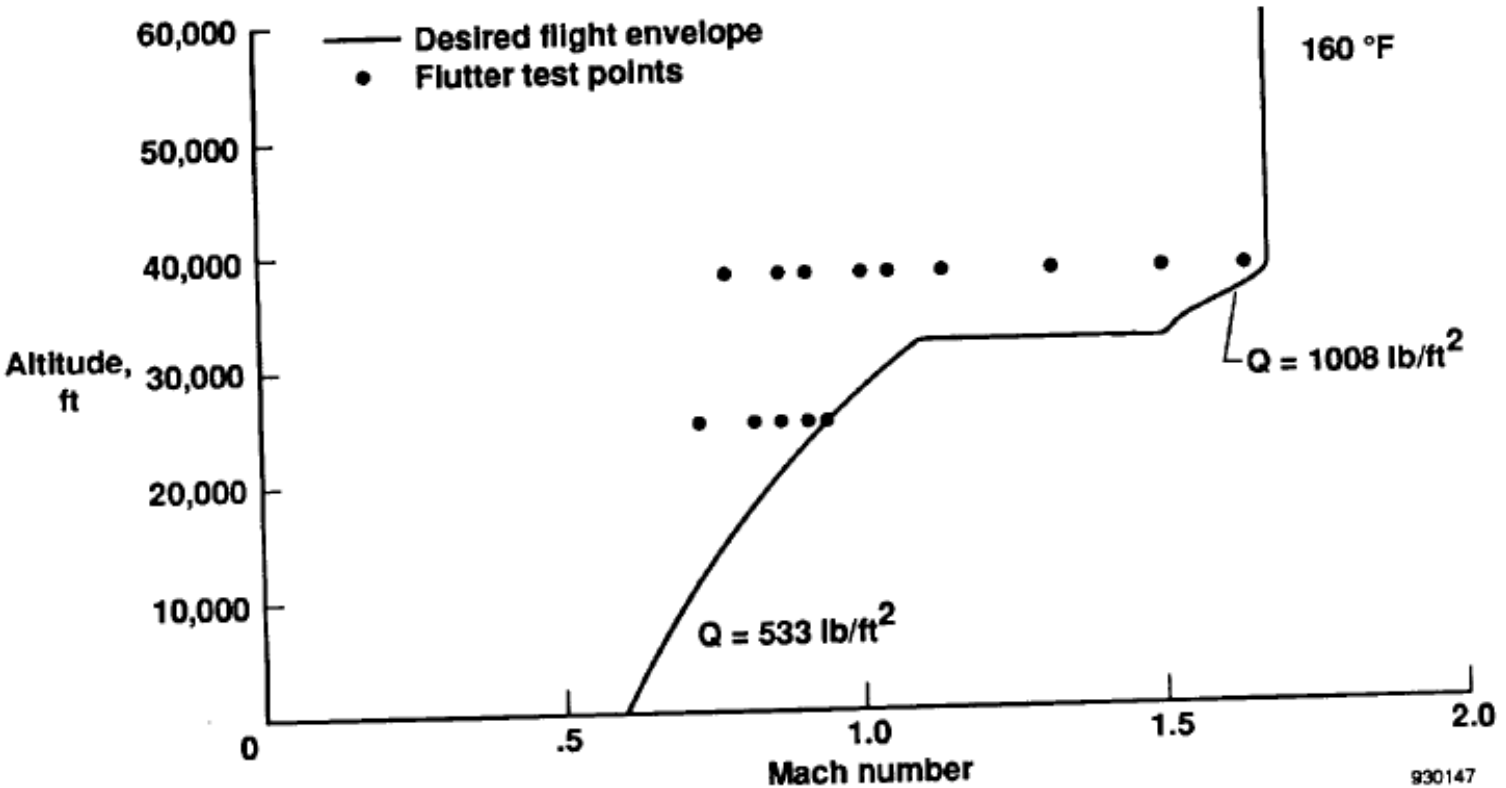

Figure 7. Flight flutter test points and desired flight envelope.

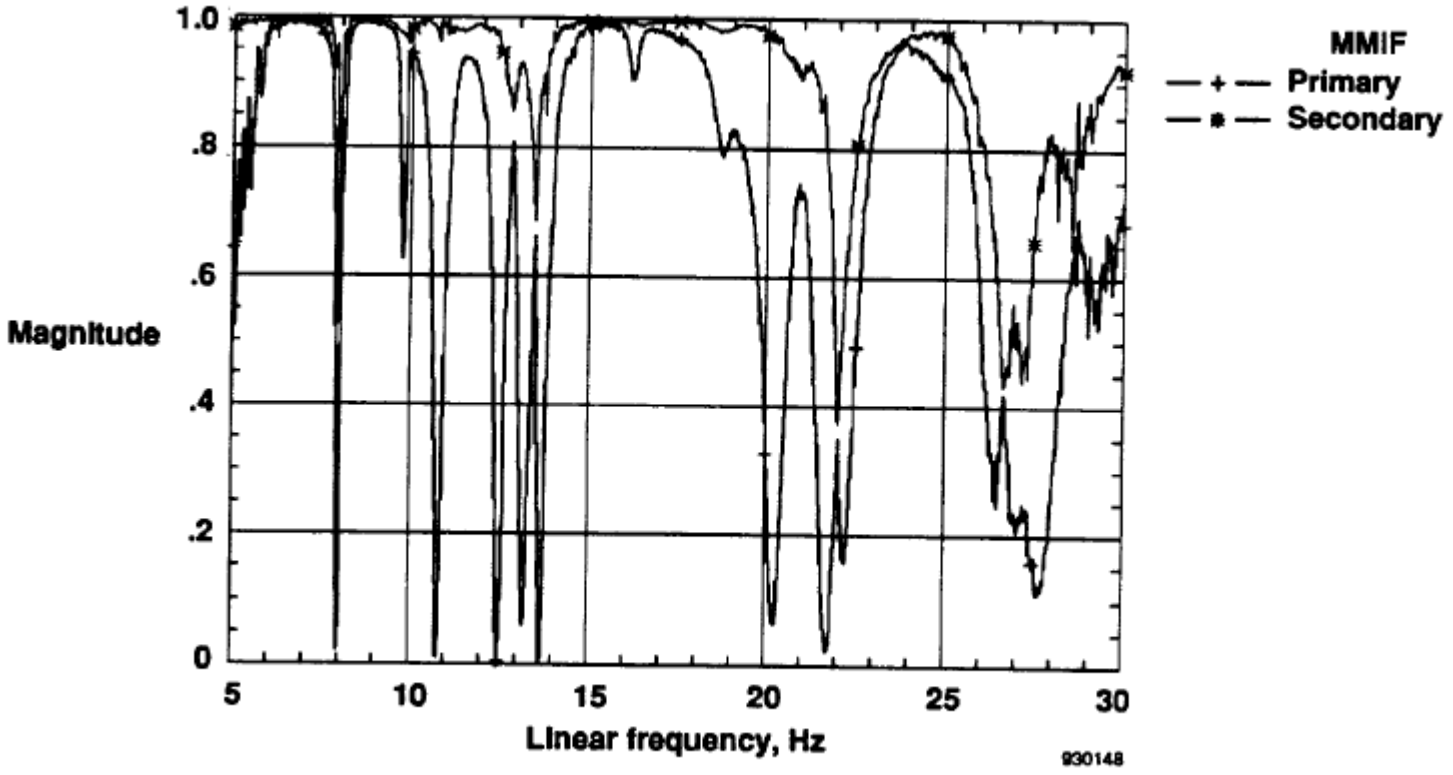

Figure 8. Baseline aircraft MMIF.

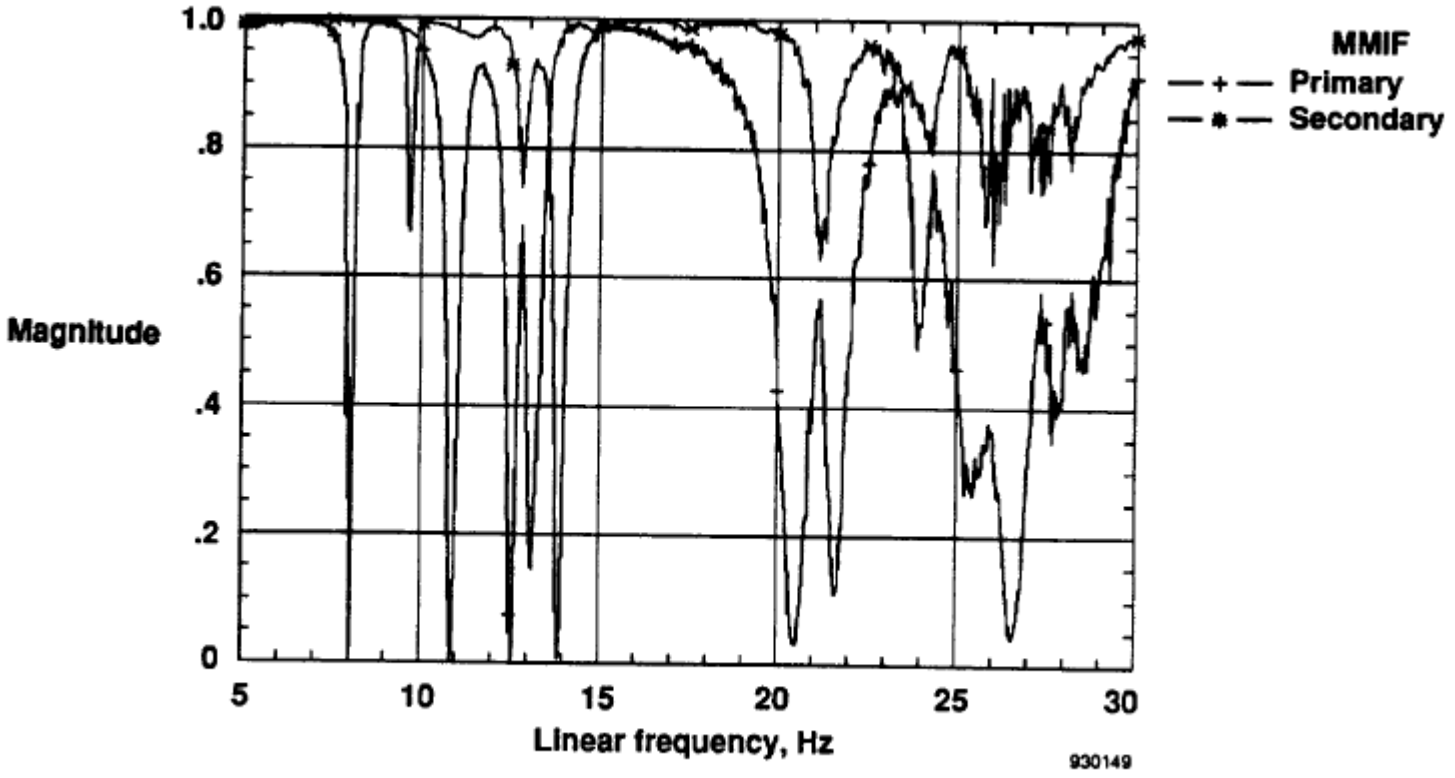

Figure 9. Modified aircraft MMIF.

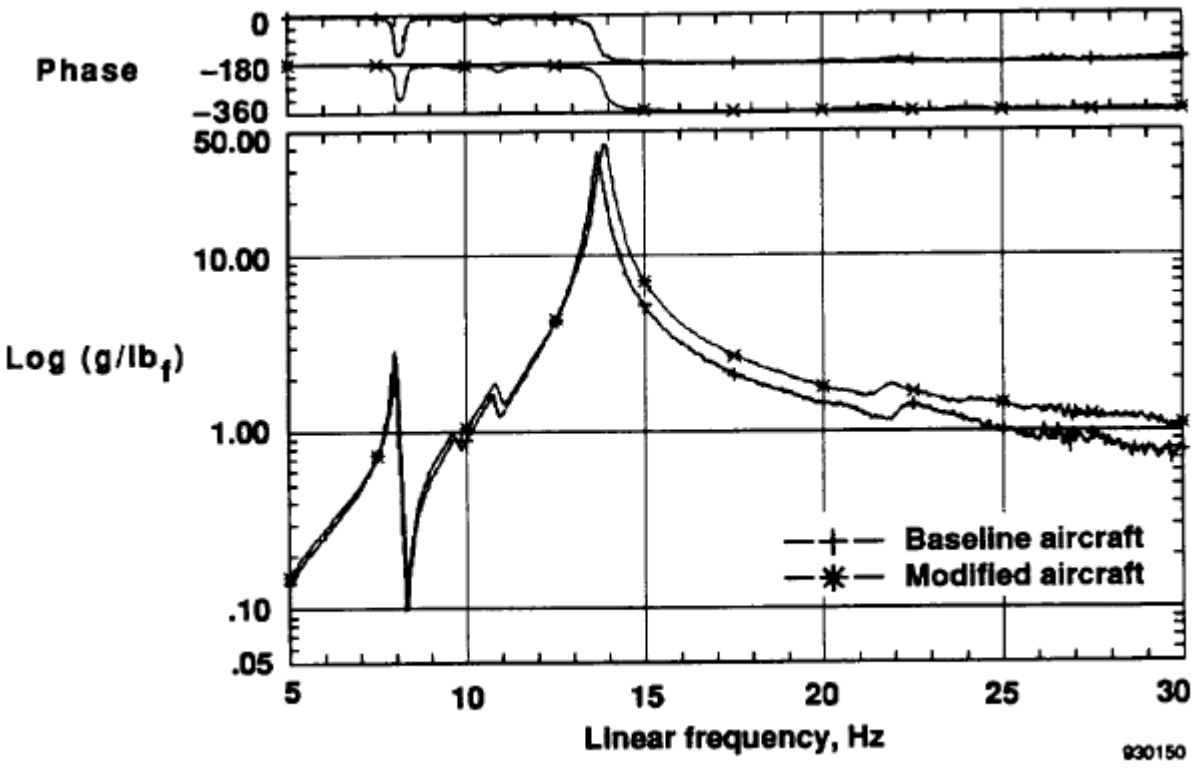

Figure 10. Left-wing driving point accelerometer FRF.

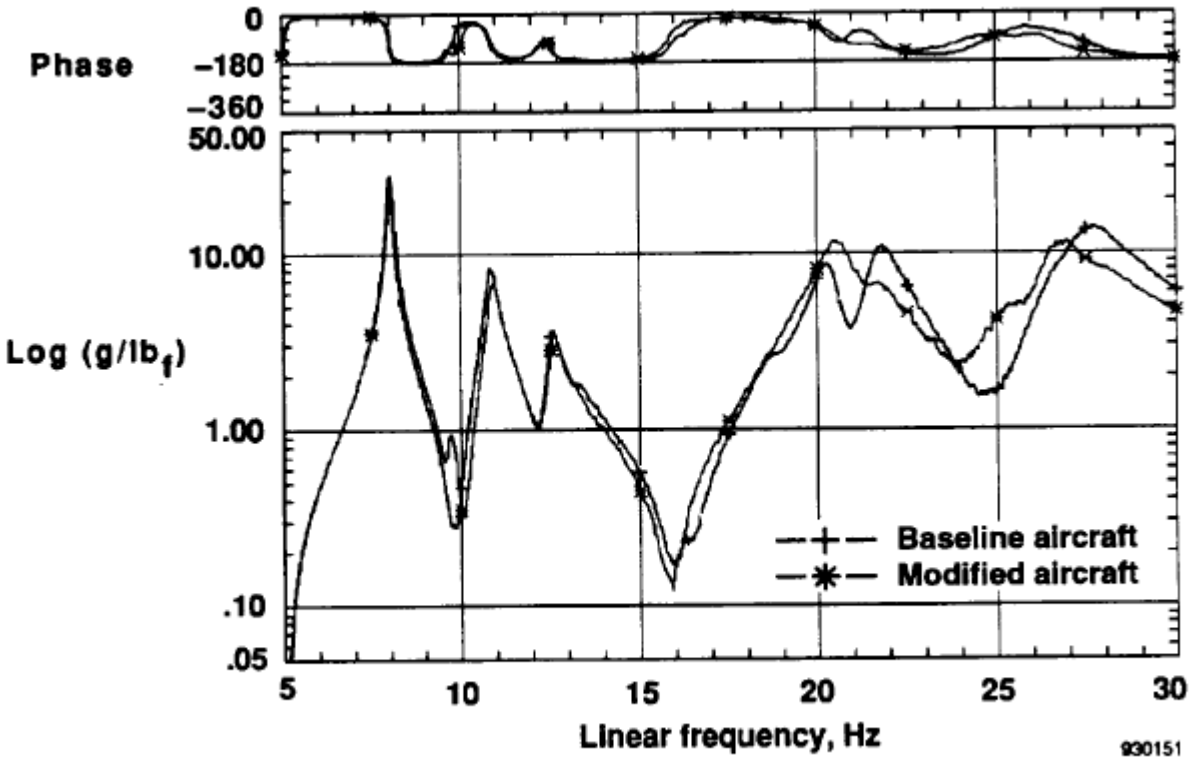

Figure 11. Right-wing driving point accelerometer FRF.

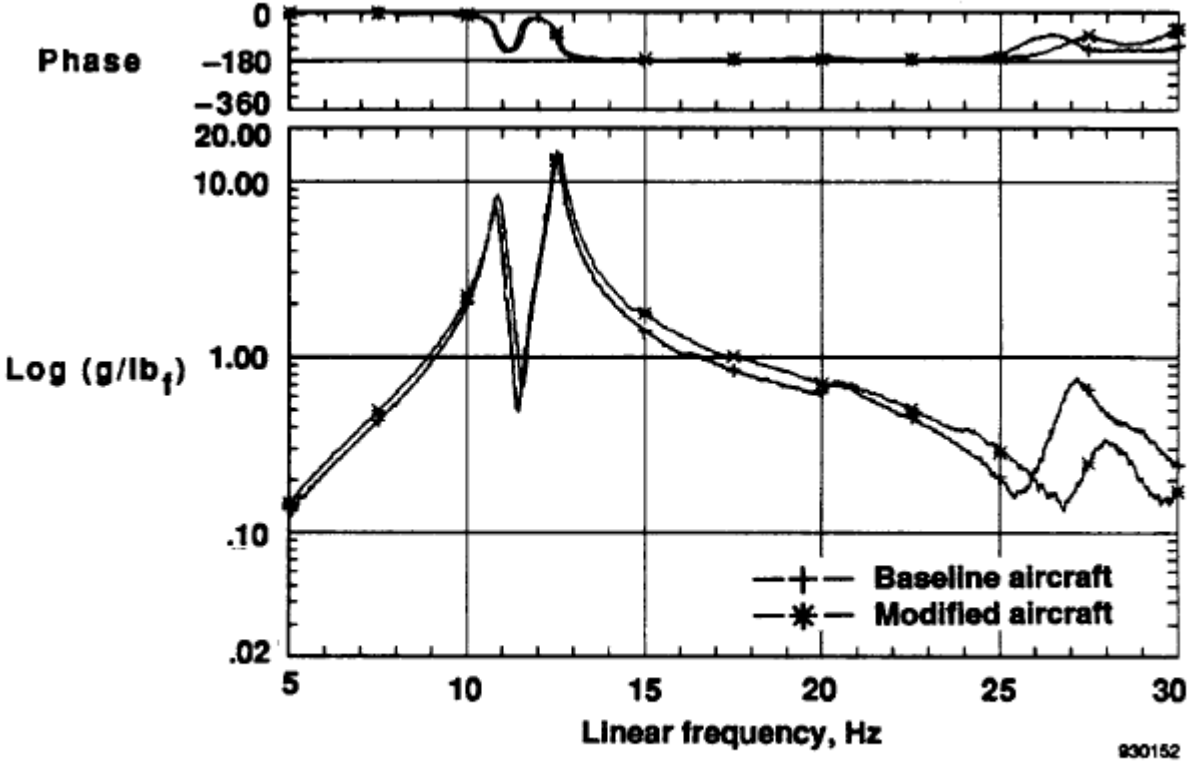

Figure 12. Vertical-tail driving point accelerometer FRF.

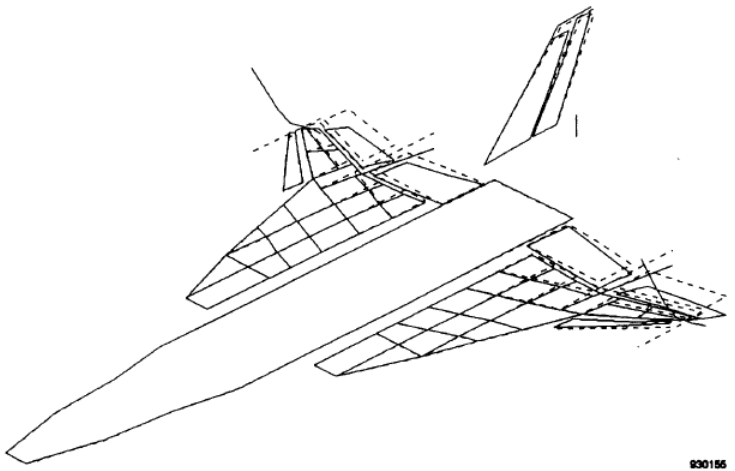

(a) Baseline, 13.69 Hz.

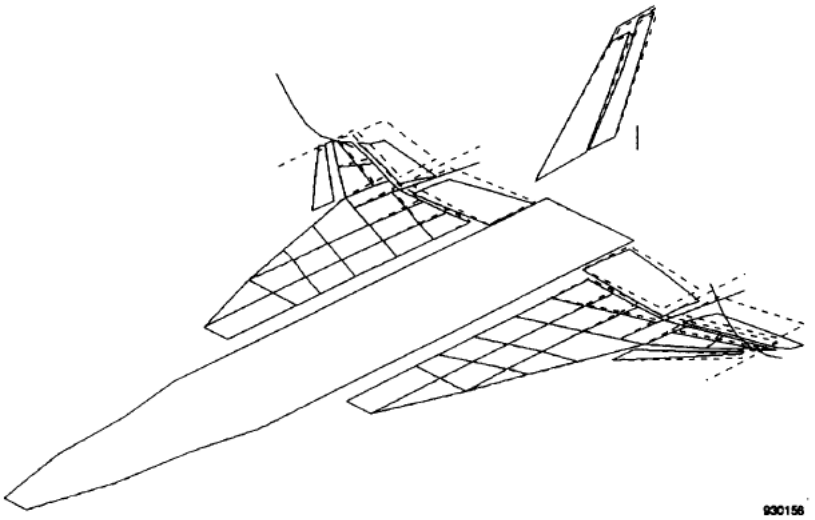

(b) Modified, 13.88 Hz.

Figure 14. Aircraft mode shapes, symmetric launcher rail bending.

Table 3. Flutter analysis for baseline aircraft (from Ref. 10).

			Subsonic (Mach 0.9)		Subsonic (Mach 0.9)		Supersonic (Mach 1.2)		Supersonic (Mach 1.2)	
			Symmetric		Antisymmetric		Symmetric		Antisymmetric	
Fuselage fuel	Wing fuel	Wingtip store	Minimum velocity, KEAS	Frequency, Hz	Minimum velocity, KEAS	Frequency, Hz	Minimum velocity, KEAS	Frequency, Hz	Minimum velocity, KEAS	Frequency, Hz
Full	Empty	Clean	1022	13	939	24.6	1260	28.8	880	25.9
Full	Half full	Clean	1084	12.2	863	24	1164	28	835	26.1
Full	Empty	Launcher	1047	13.3	924	23.9	1377	18.1	874	24.5
Full	Half full	Launcher	1162	11.5	763	23.5	1299	18.9	805	25.3
Full	Empty	Aim-9L	1165	11.8	792	23.9	1333	12.5	965	26
Full	Half full	Aim-9L	1146	11.3	774	24.8	1329	12.3	953	29.2

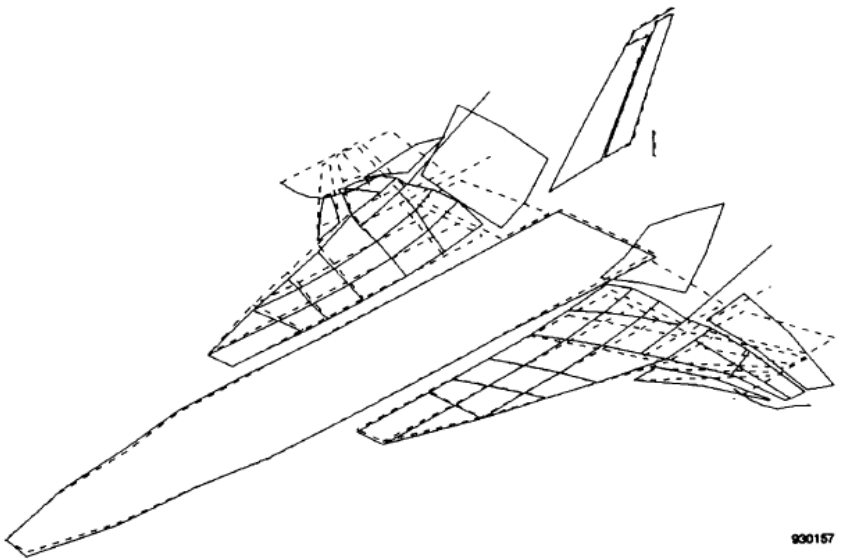

(a) Baseline, 21.74 Hz.

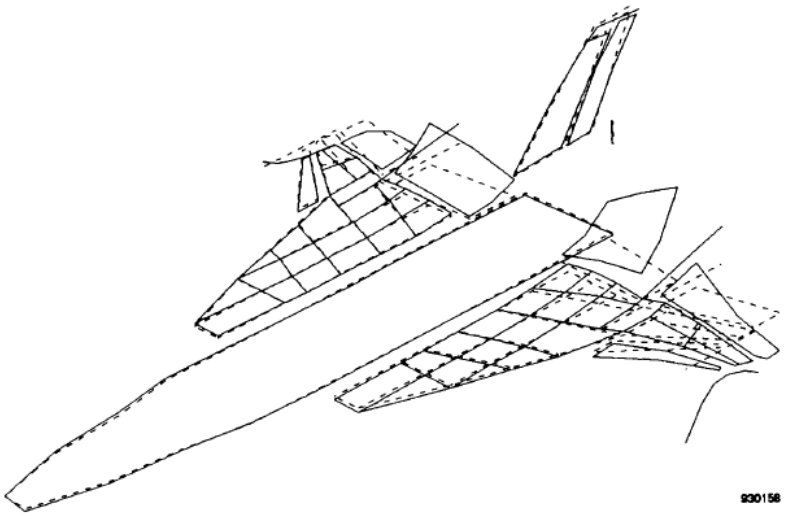

(b) Modified, 21.53 Hz.

Figure 15. Aircraft mode shapes, symmetric control surface mode 1.

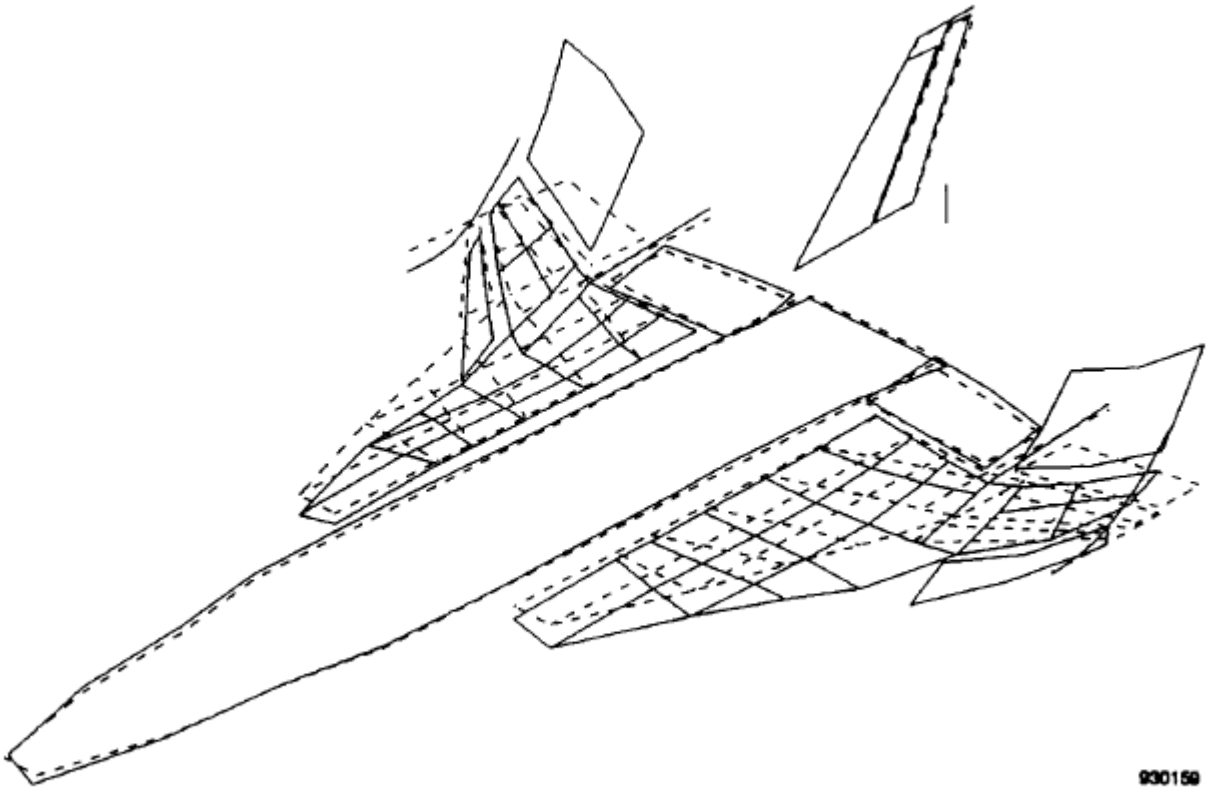

(a) Baseline, 26.42 Hz.

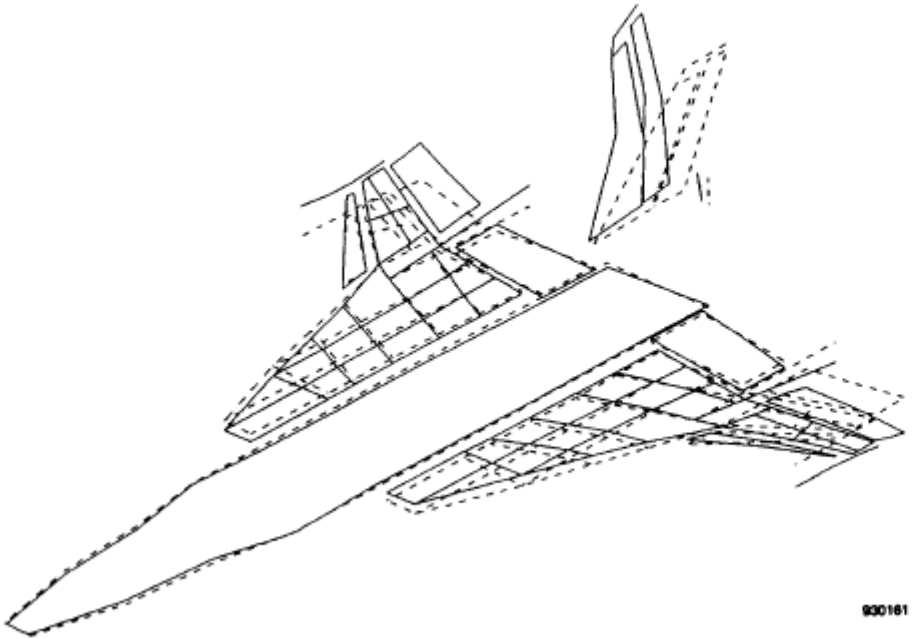

(a) Baseline, 10.79 Hz.

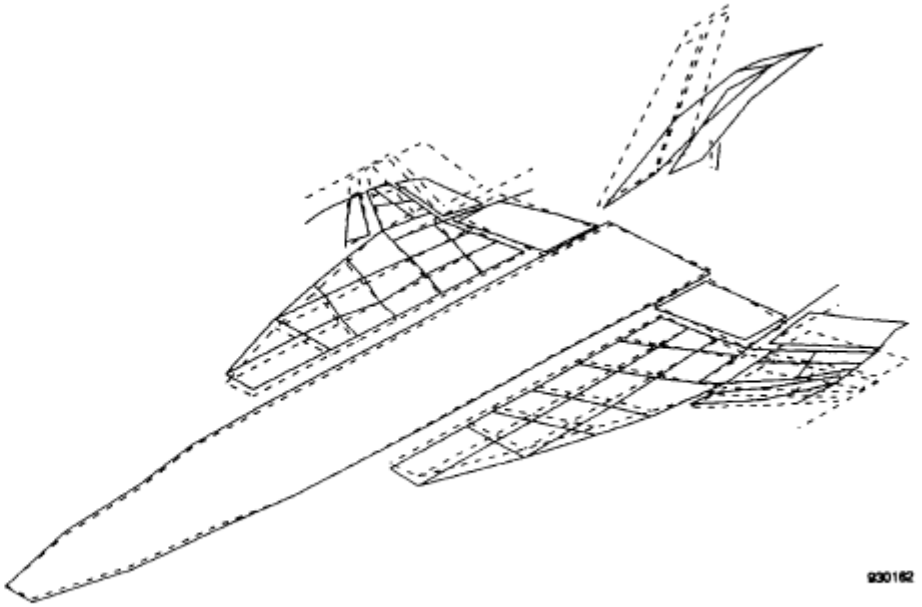

(b) Modified, 10.90 Hz.

Figure 17. Aircraft mode shapes, antisymmetric wing bending.

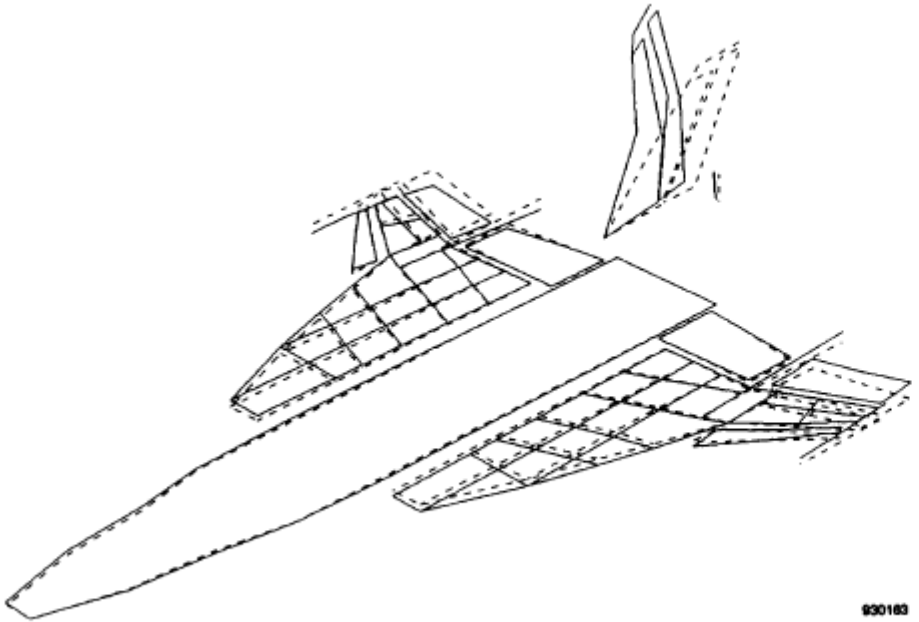

(a) Baseline, 12.48 Hz.

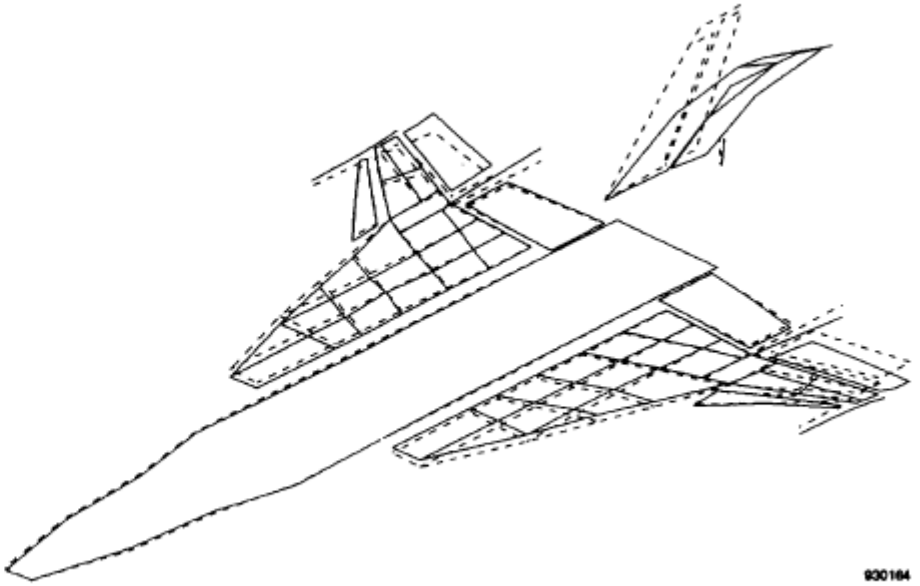

(b) Modified, 12.56 Hz.

Figure 18. Aircraft mode shapes, vertical tail bending.

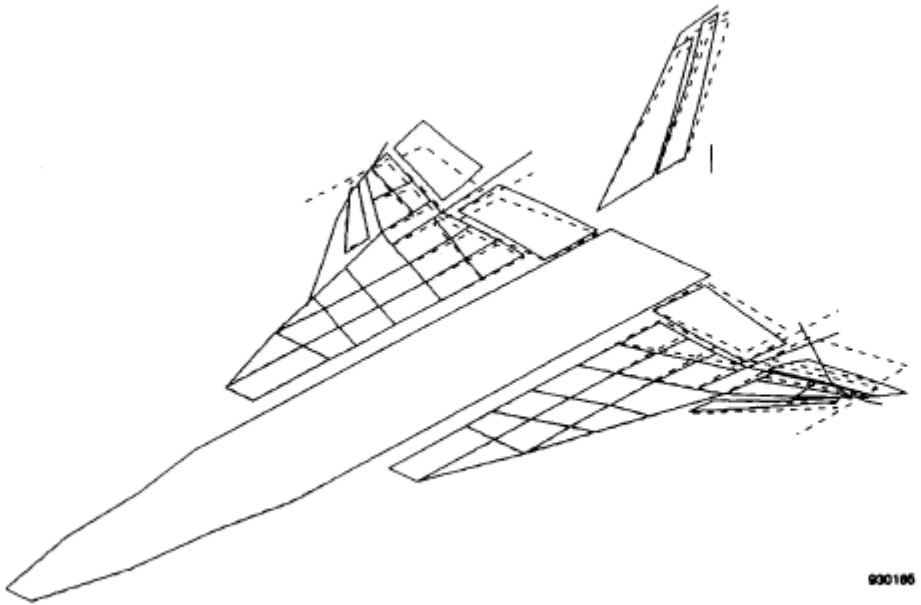

(a) Baseline, 13.24 Hz.

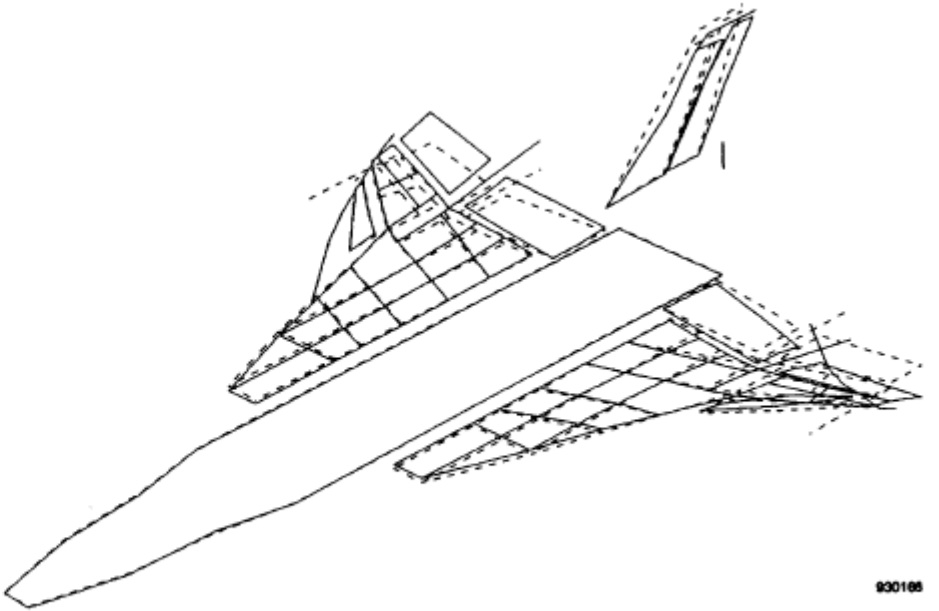

(b) Modified, 13.23 Hz.

Figure 19. Aircraft mode shapes, antisymmetric launcher rail bending.

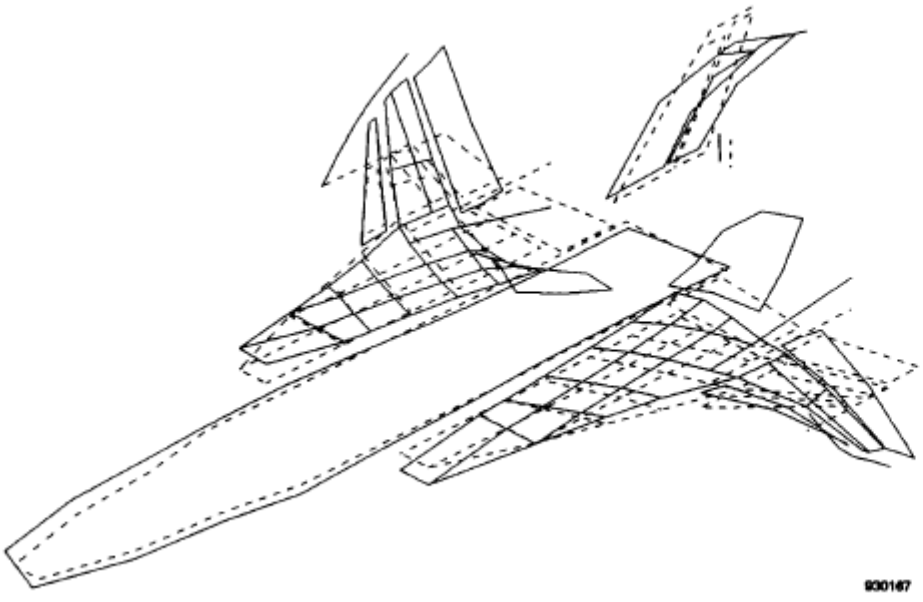

(a) Baseline, 20.36 Hz.

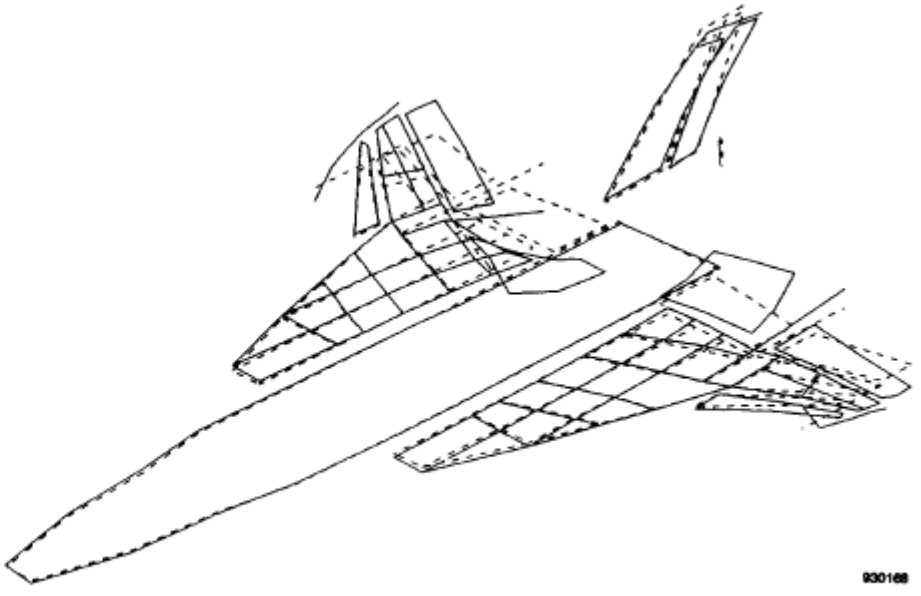

(b) Modified, 20.57 Hz.

Figure 20. Aircraft mode shapes, antisymmetric control surface mode 1.

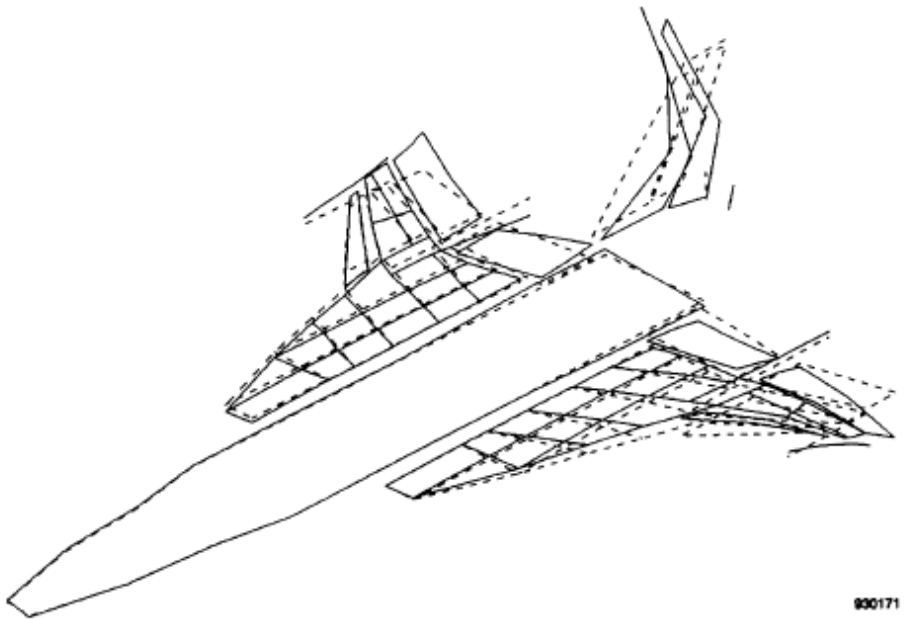

(a) Baseline, 27.05 Hz.

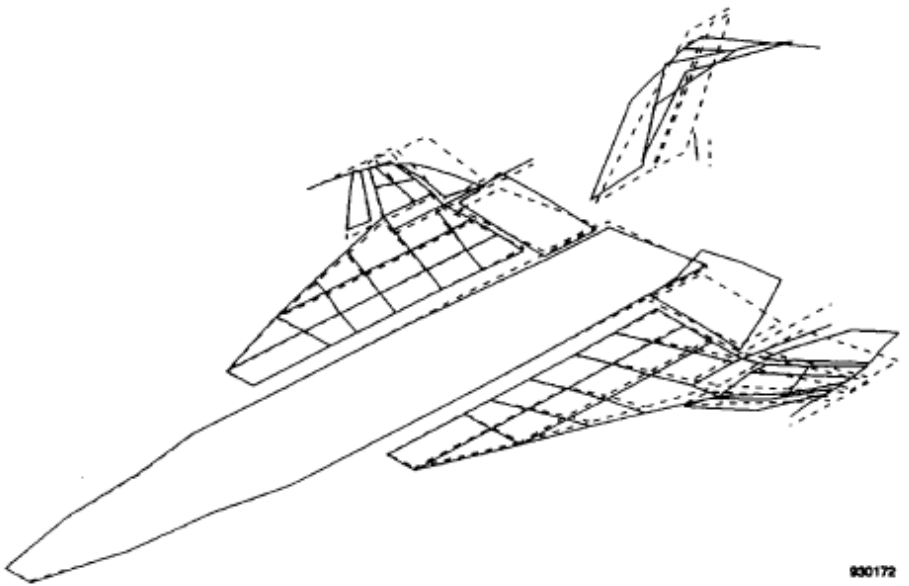

(b) Modified, 27.81 Hz.

Figure 22. Aircraft mode shapes, antisymmetric control surface mode 3.

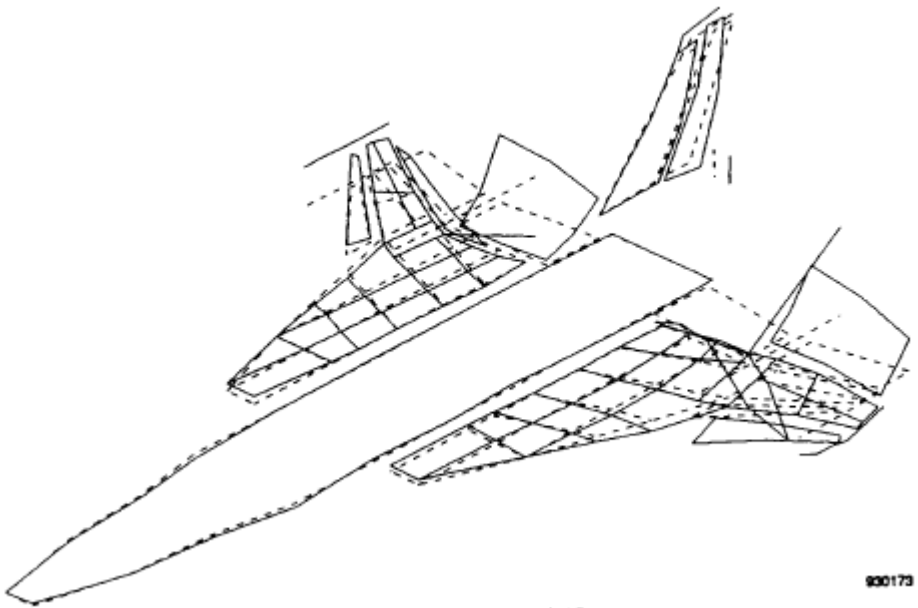

(a) Baseline, 28.78 Hz.

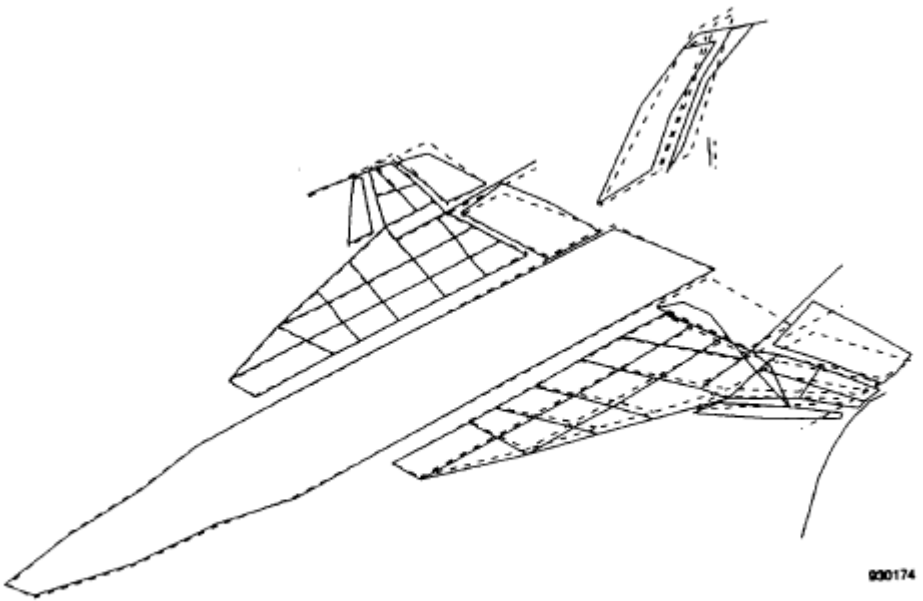

(b) Modified, 28.65 Hz.

Figure 23. Aircraft mode shapes, antisymmetric control surface mode 4.

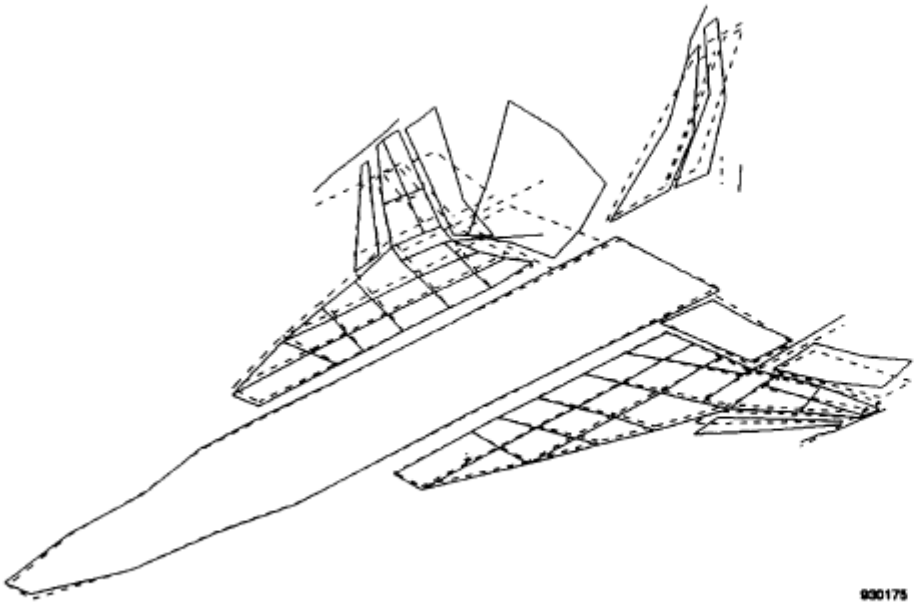

(a) Baseline, 27.17 Hz.

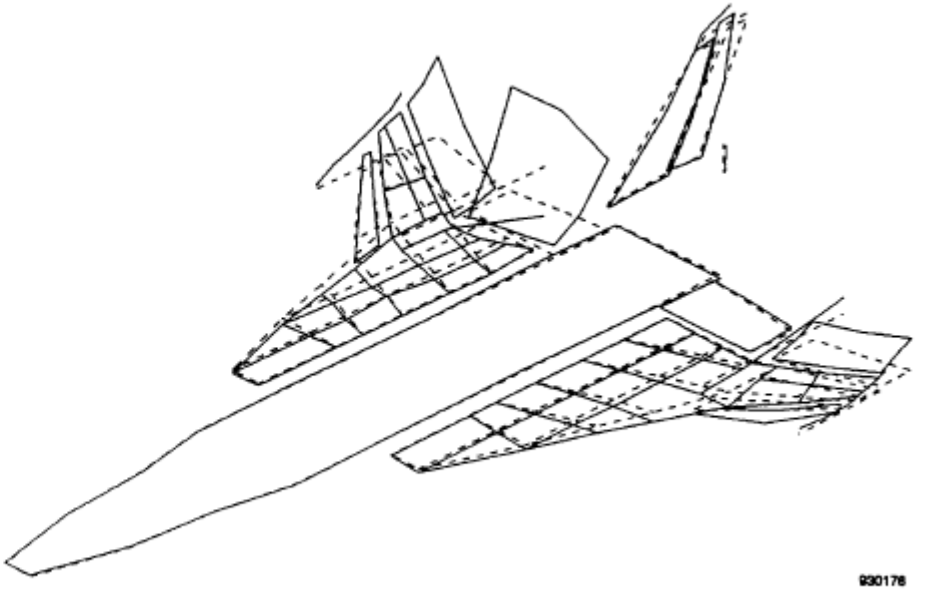

(b) Modified, 26.62 Hz.

Figure 24. Aircraft mode shapes, asymmetric control surface mode 1.

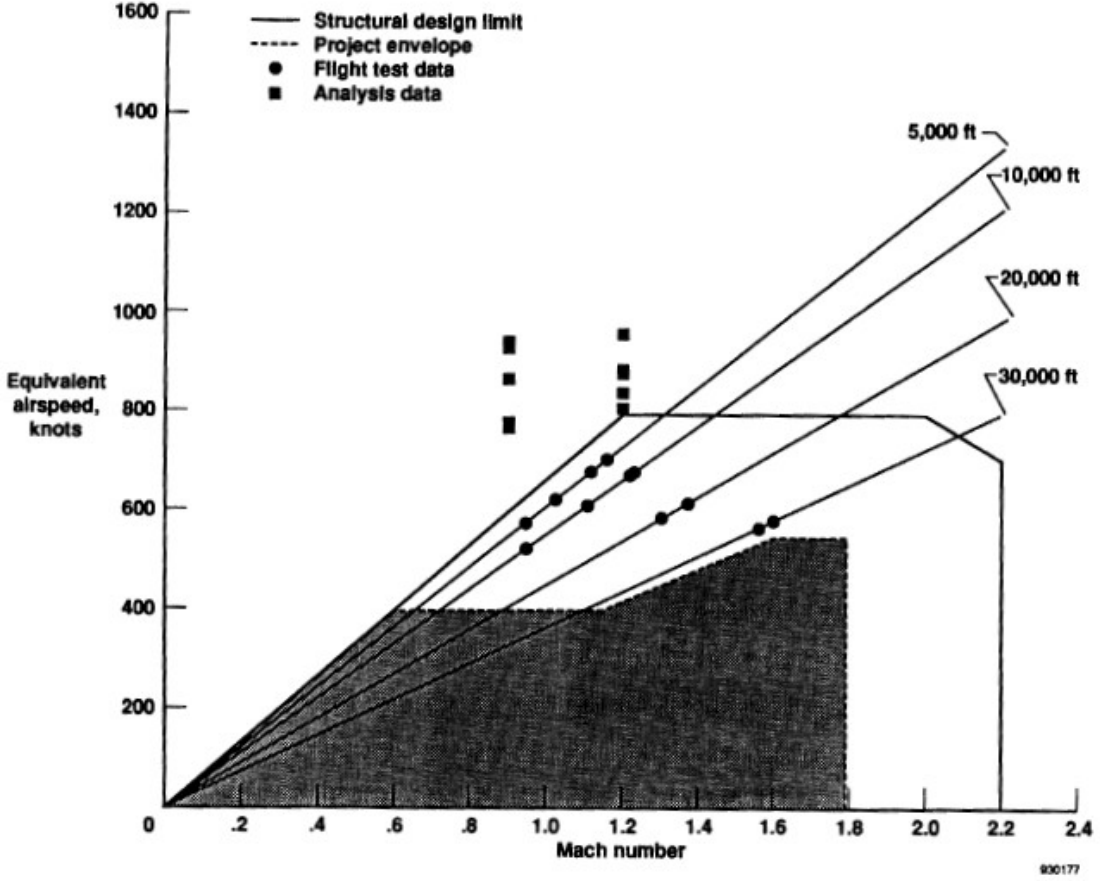

Figure 25. Summary of manufacturer's F-16XL flight and analysis test data.

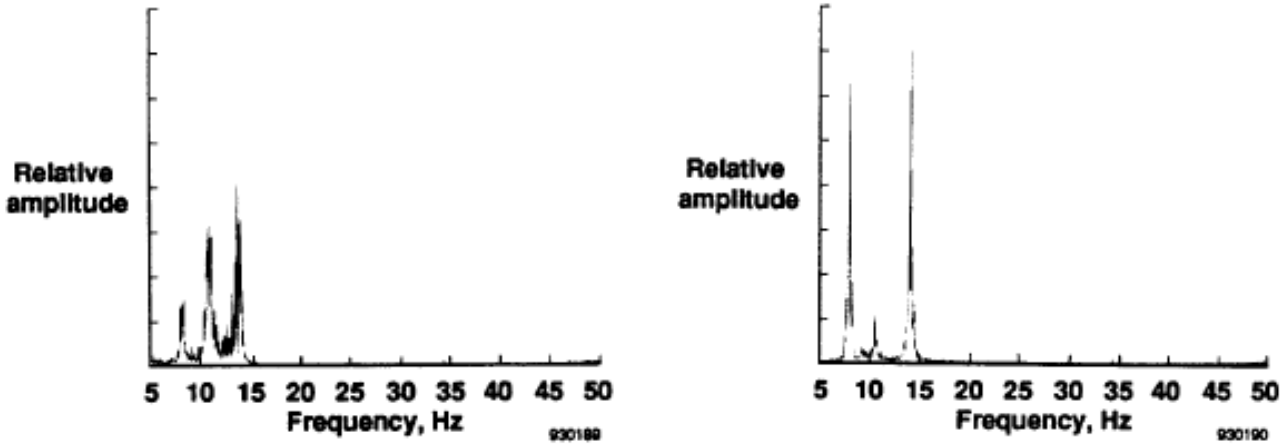

(a) 25,000 ft. (b) 38,000 ft.

Figure 26 Left-wing forward accelerometer spectrum.

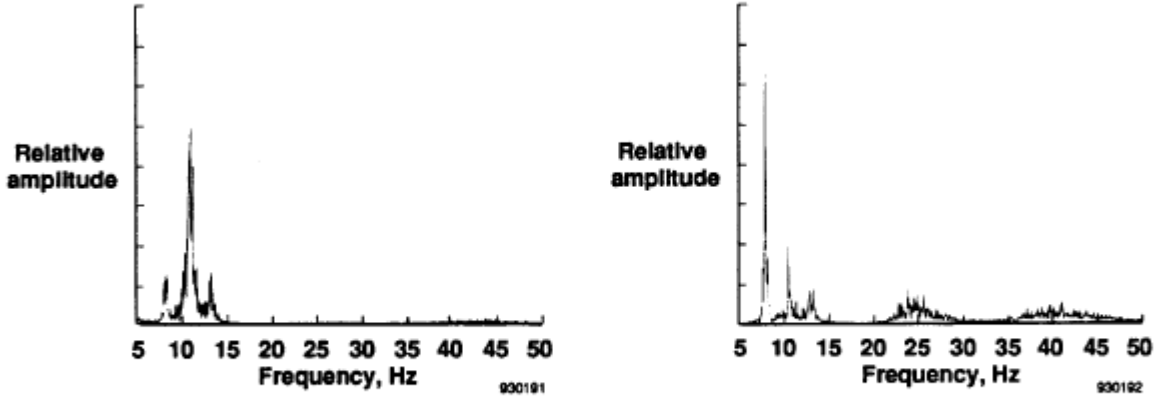

(a) 25,000 ft. (b) 38,000 ft.

Figure 27. Right-wing forward accelerometer spectrum.

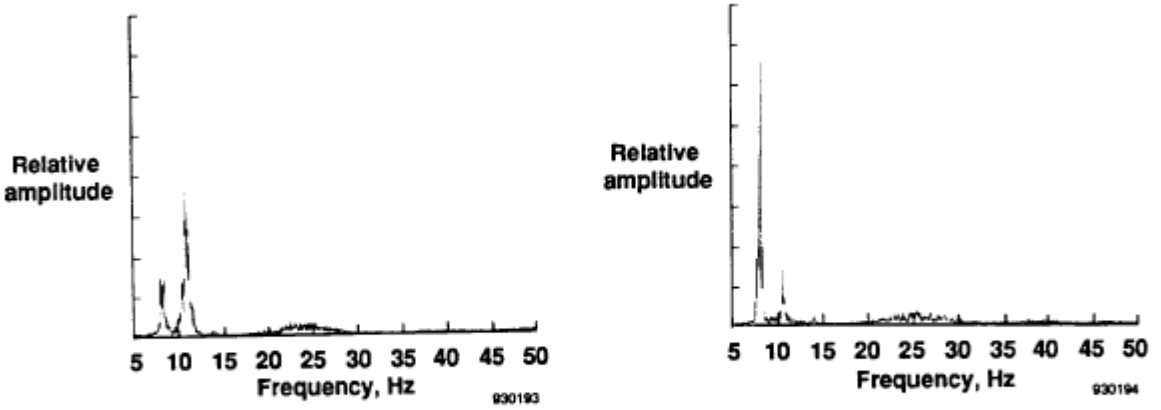

(a) 25,000 ft. (b) 38,000 ft.

Figure 28. Left-wing aft accelerometer spectrum.

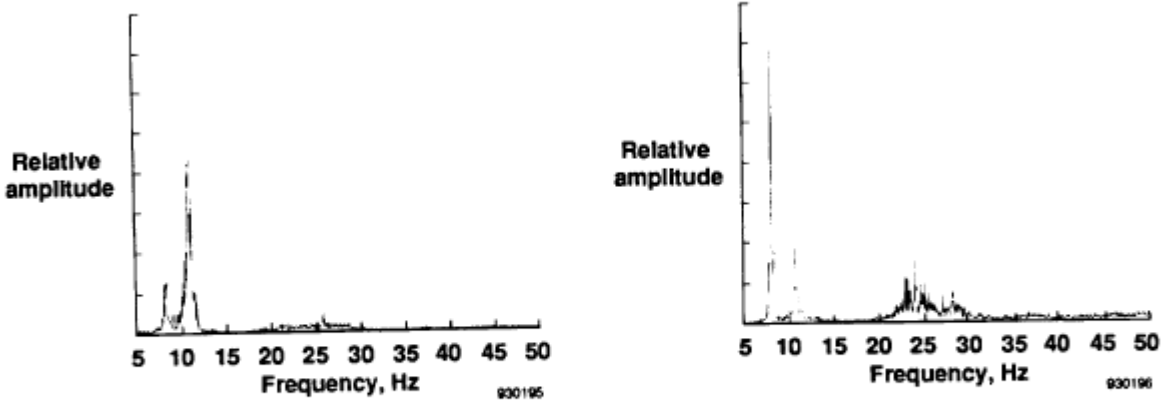

(a) 25,000 ft. (b) 38,000 ft.

Figure 29. Right-wing aft accelerometer spectrum.

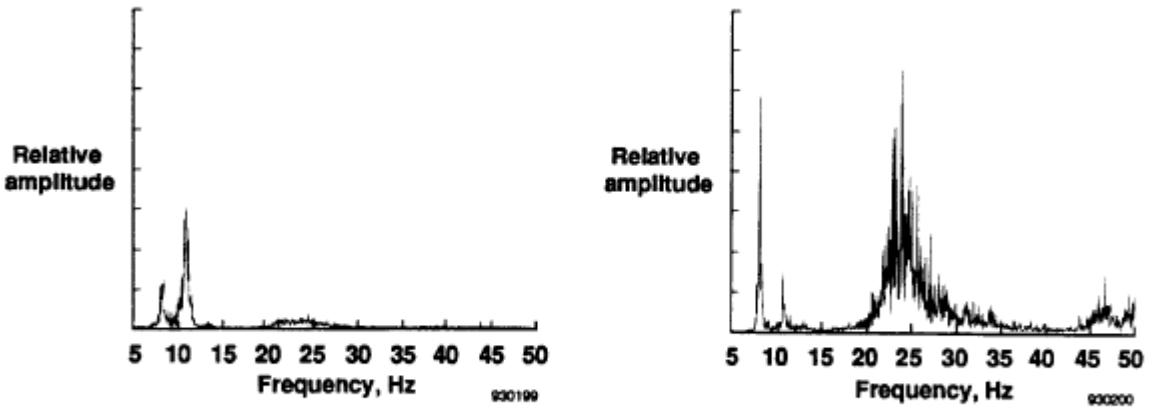

(a) 25,000 ft. (b) 38,000 ft.

Figure 31. Right-aileron beam accelerometer spectrum.

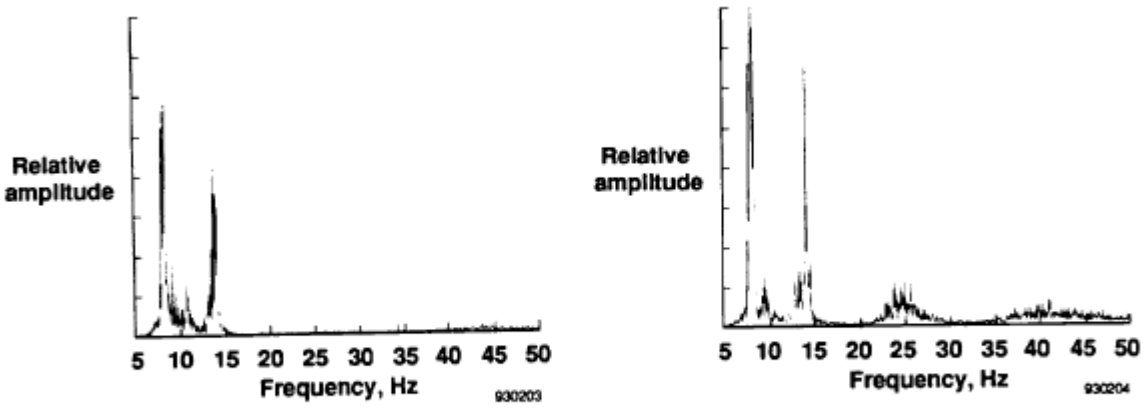

(a) 25,000 ft. (b) 38,000 ft.

Figure 33. Accelerometer spectrum for left- plus right-wing forward.

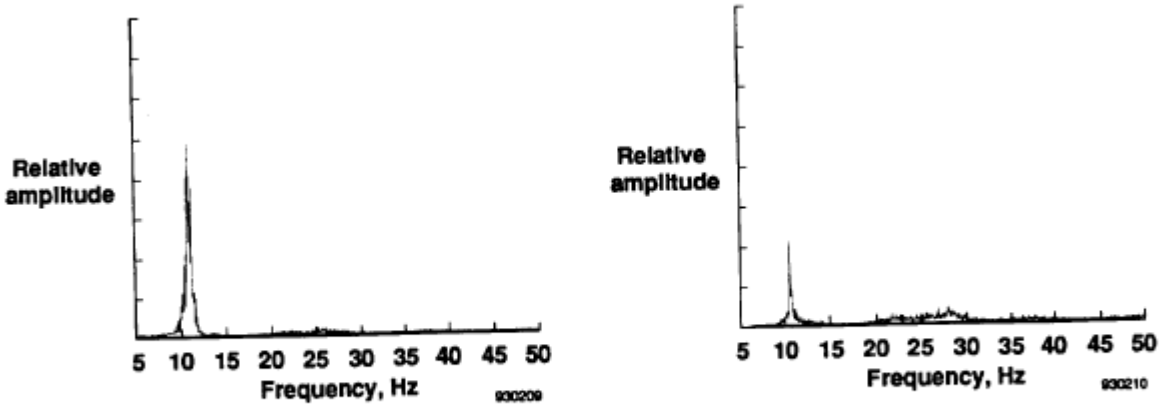

(a) 25,000 ft. (b) 38,000 ft.

Figure 36. Accelerometer spectrum for left- minus right-wing aft.

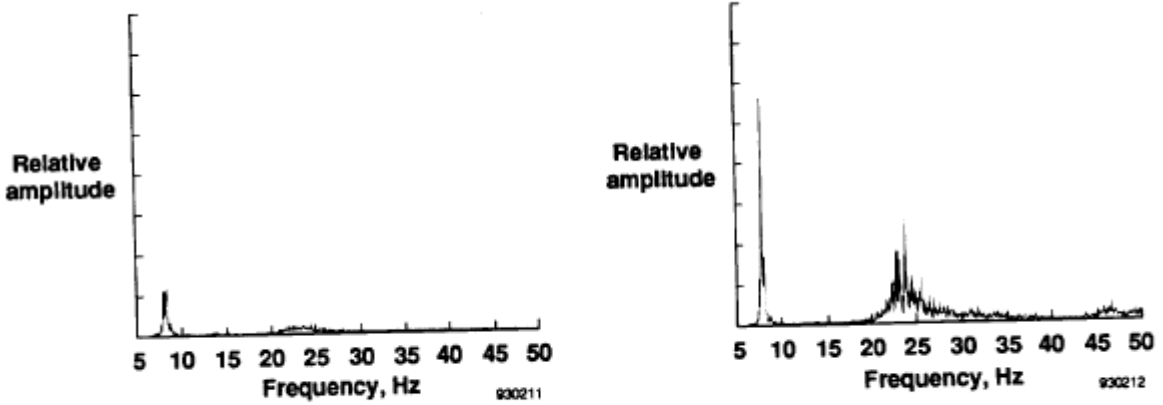

(a) 25,000 ft. (b) 38,000 ft.

Figure 37. Accelerometer spectrum for left- plus right-aileron beam.

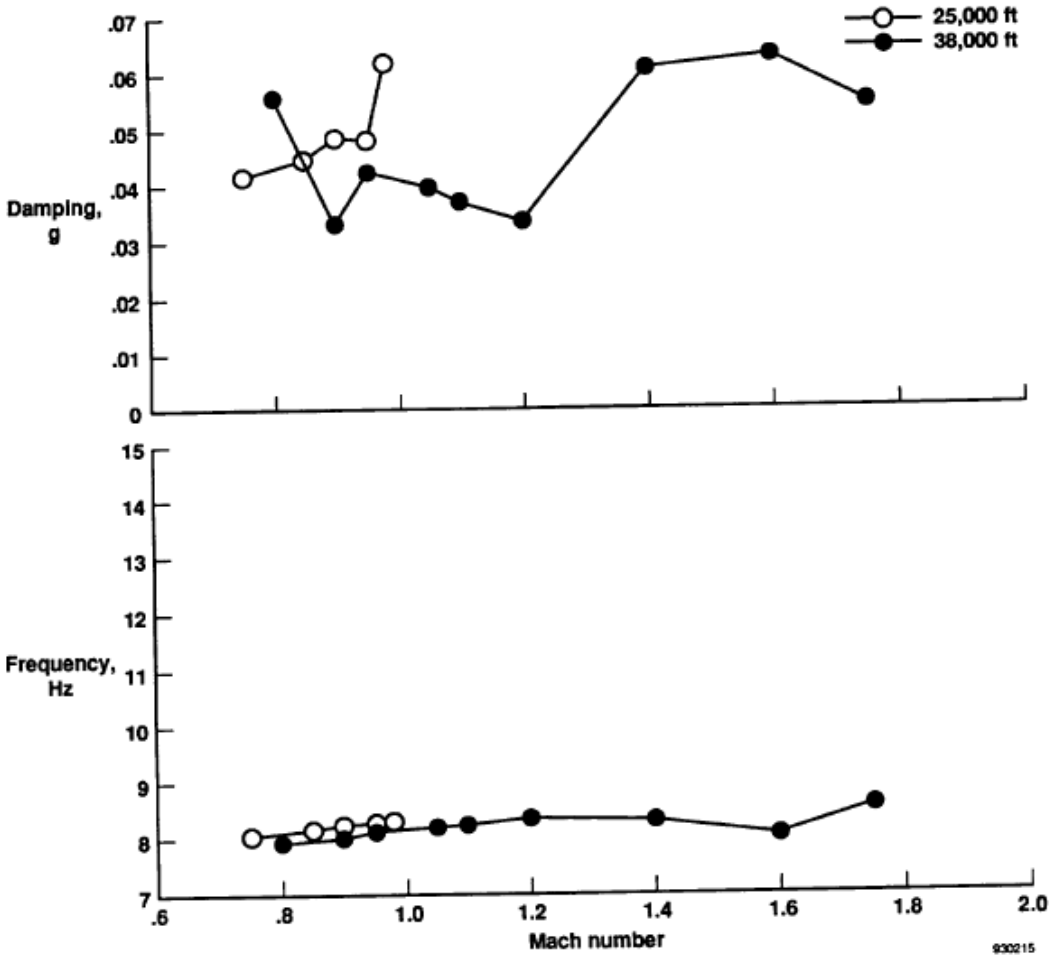

Figure 39. Symmetric wing bending flight test data.

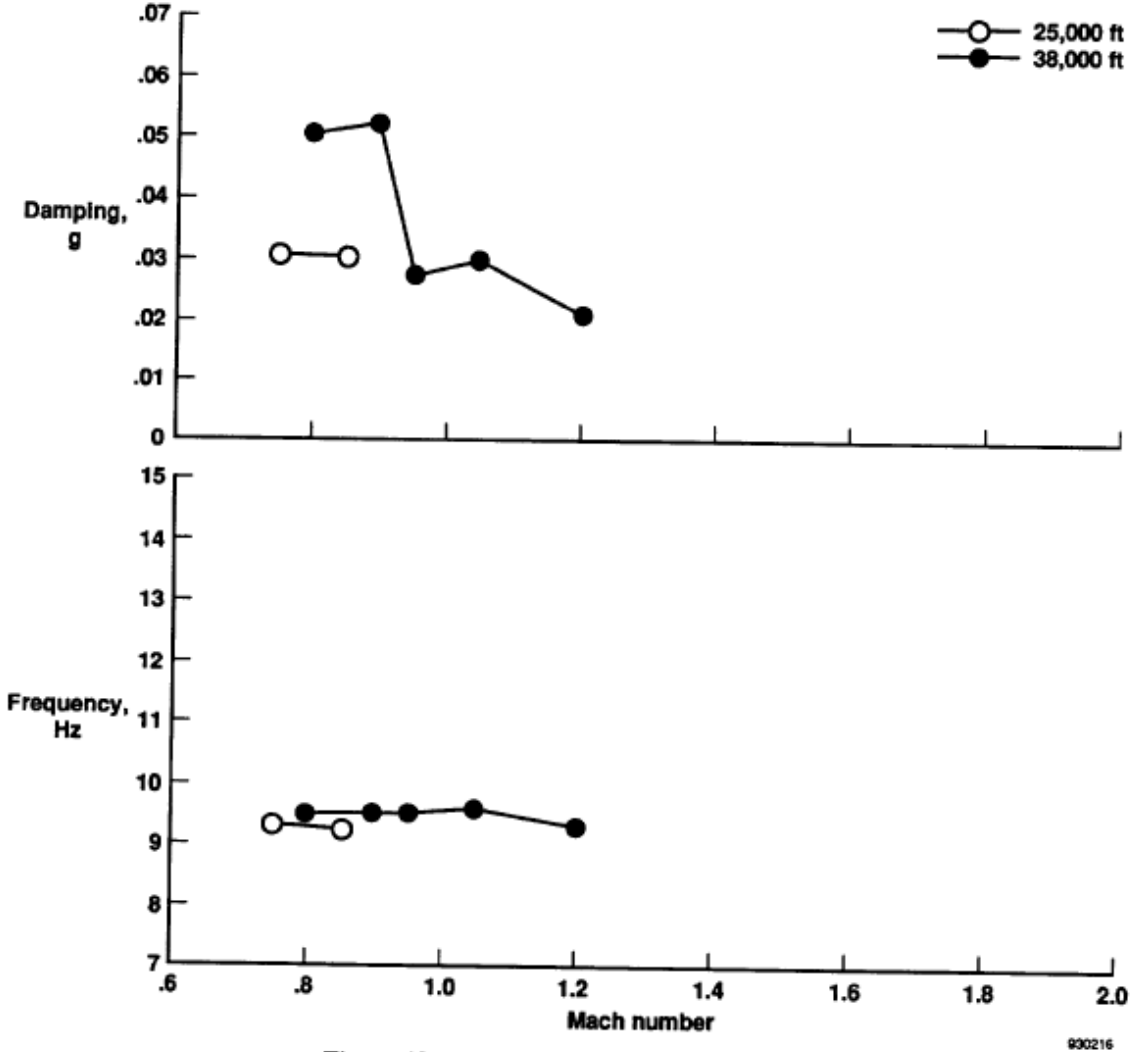

Figure 40. Fuselage bending flight test data.

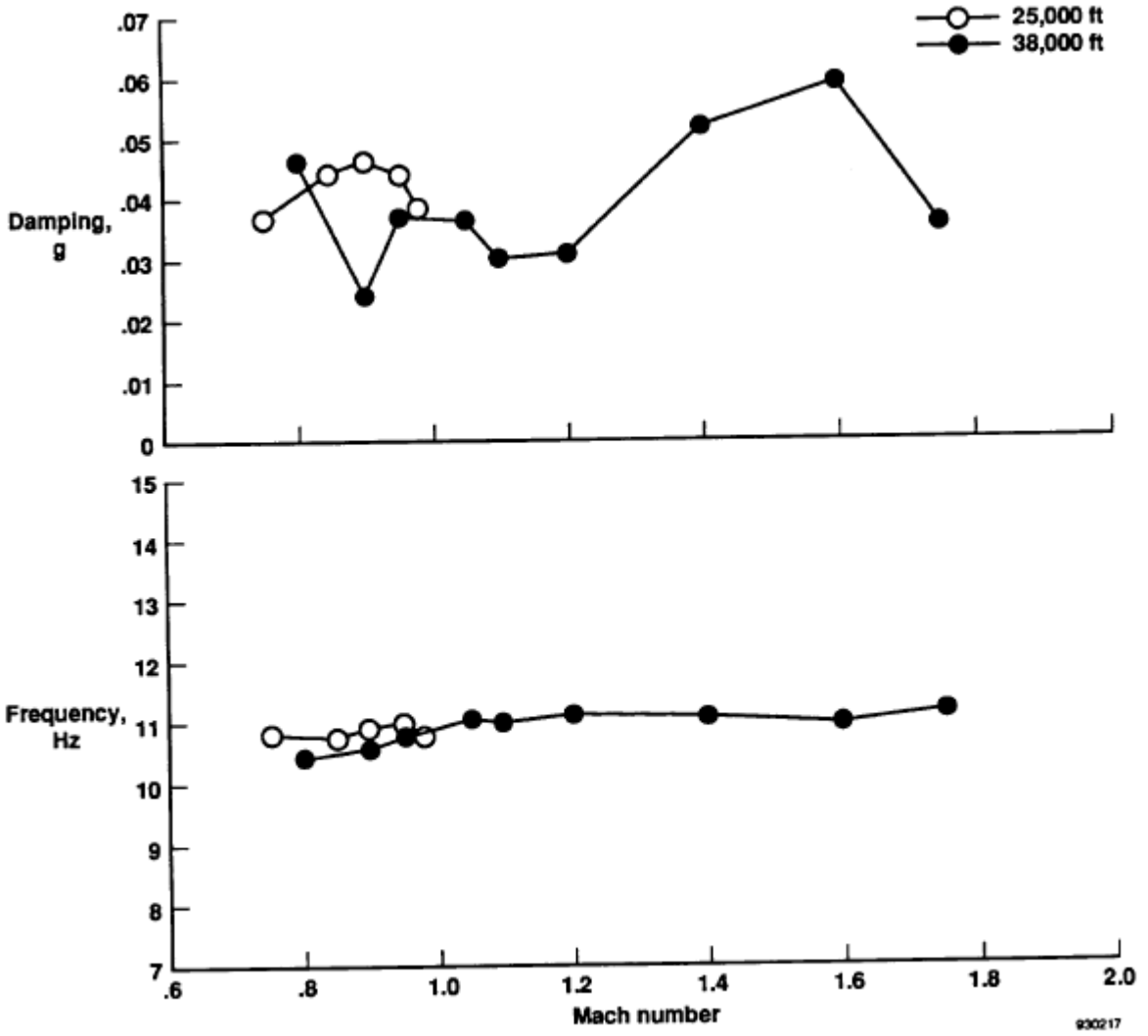

Figure 41. Antisymmetric wing bending flight test data.

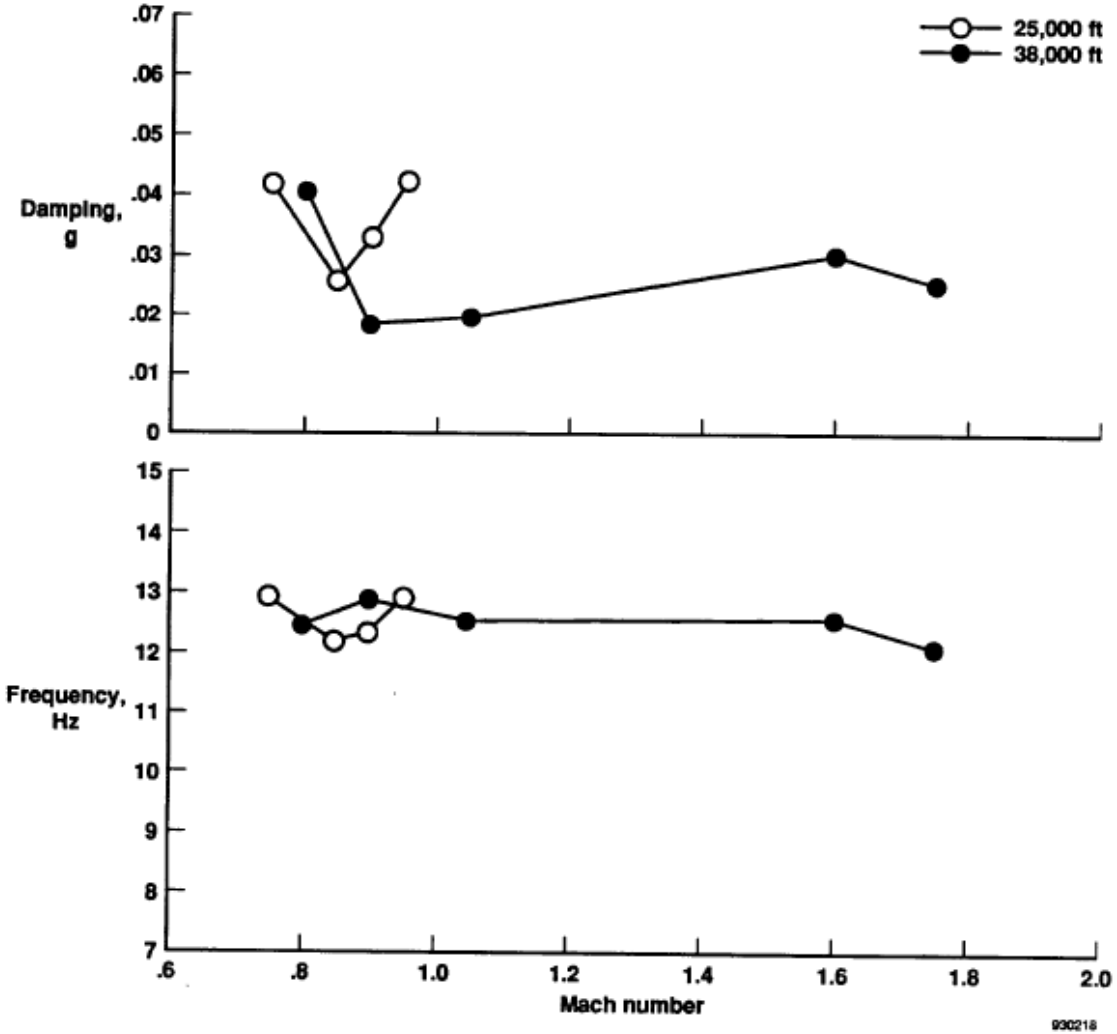

Figure 42. Vertical-tail bending flight test data.

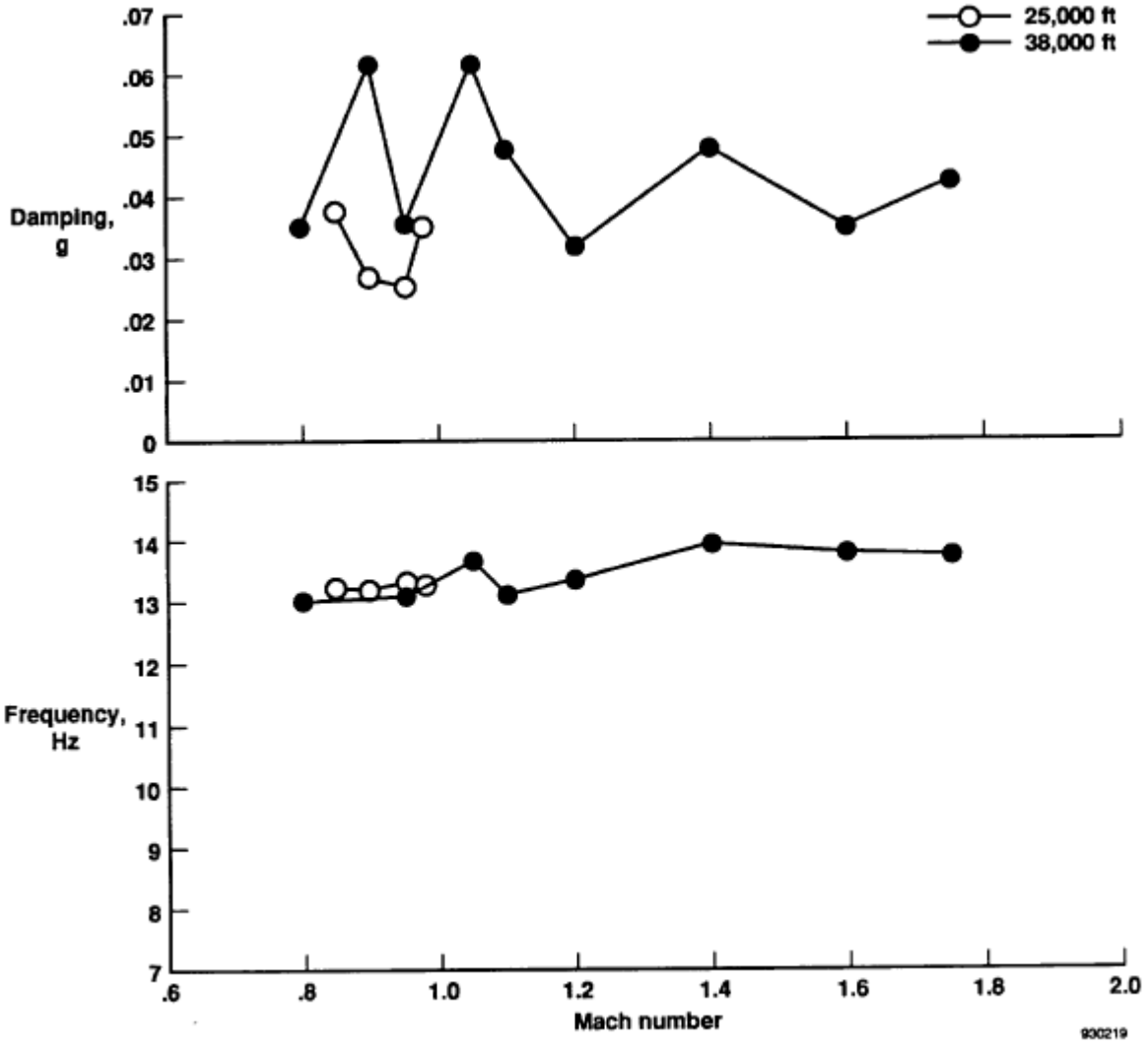

Figure 43. Antisymmetric launcher bending flight test data.

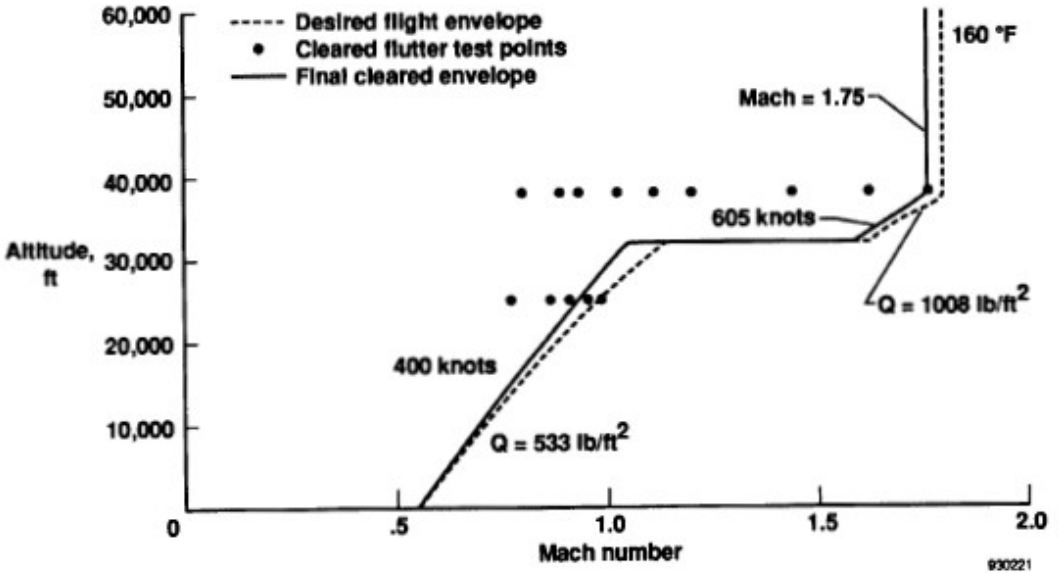

Figure 45. Final cleared flutter envelope.

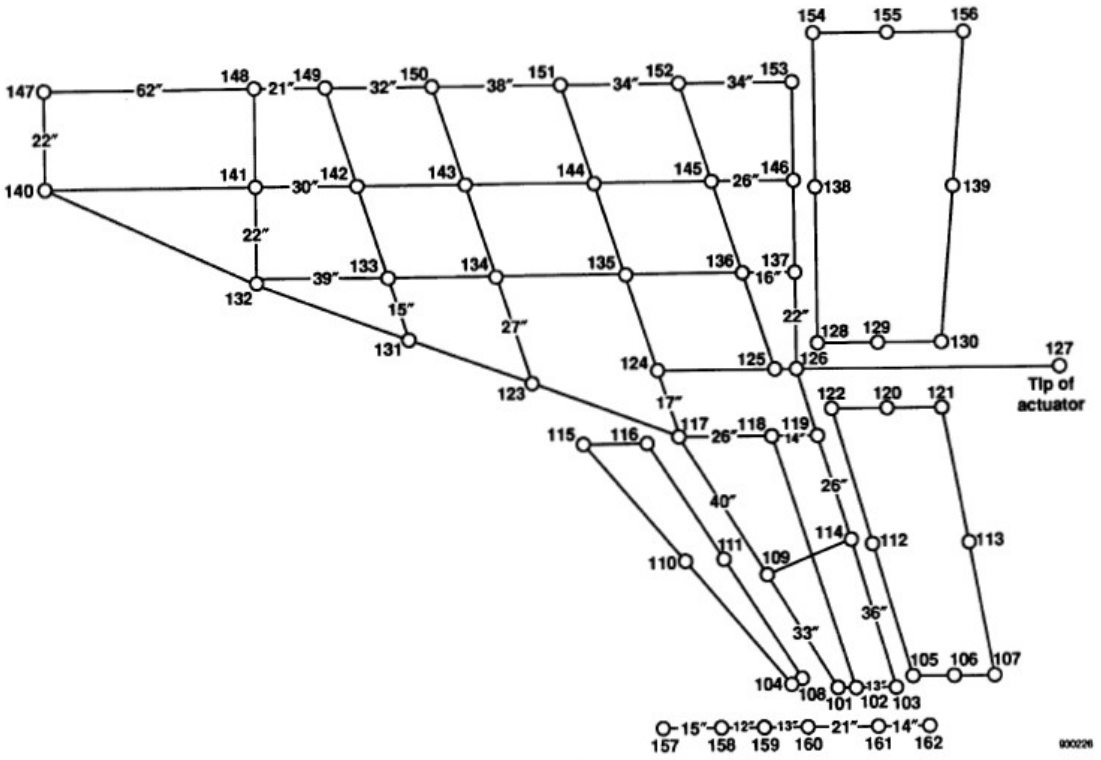
154
155
156
147
62″
148
21″
149
32″
150
38″
151
34″
152
34″
153
22″
141
30″
142
143
144
145
26″
146
138
139
140
22″
39″
133
134
135
136
137
16″
132
15″
27″
131
22″
128
129
130
127
Tip of actuator
124
125
126
123
17″
122
120
121
117
118
119
26″
14″
115
116
26″
40″
114
112
113
111
109
110
36″
33″
105
106
107
104
108
101
102
103
15″
12″
13″
21″
14″
157
158
159
160
161
162
900226

Figure A-1.

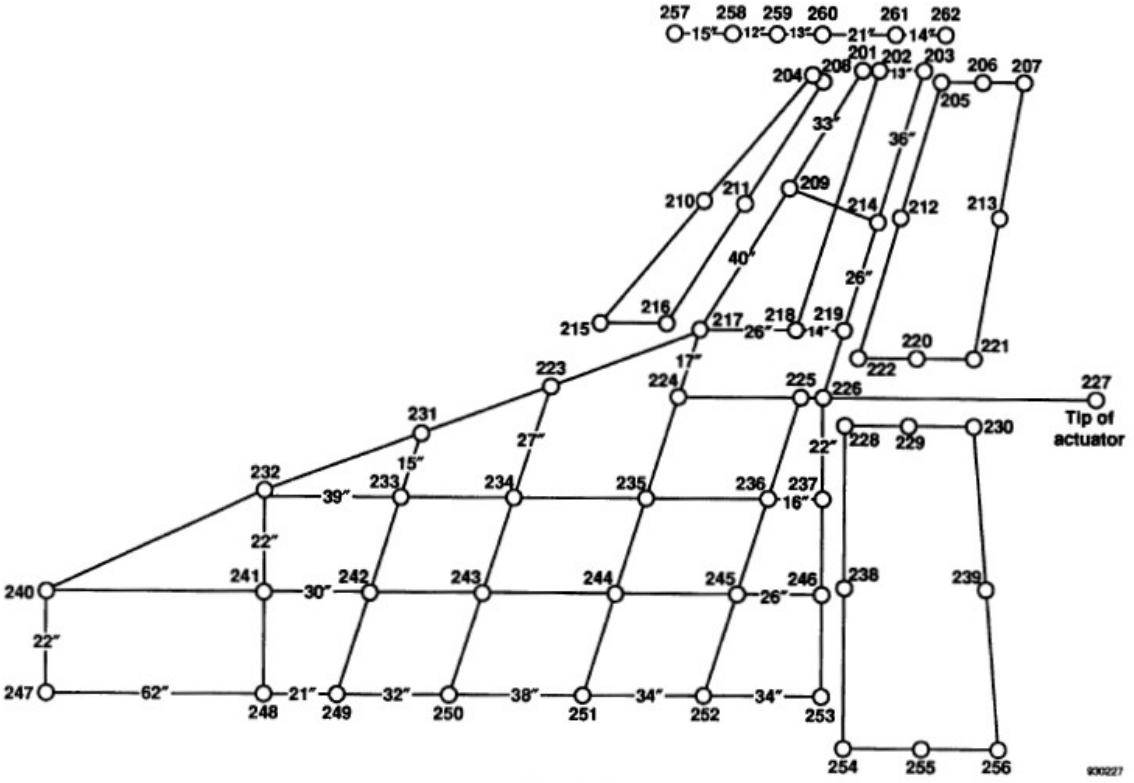
257
258
259
260
261
262
15″
12″
13″
21″
14″
201
202
203
206
207
204
208
13″
205
33″
36″
210
211
209
214
212
213
40″
26″
215
216
217
218
219
26″
14″
220
221
222
17″
223
224
225
226
227
Tip of actuator
231
27″
228
229
230
22″
15″
232
233
234
235
236
237
39″
16″
22″
241
242
243
244
245
246
238
239
240
30″
26″
22″
247
62″
248
21″
249
32″
250
38″
251
34″
252
34″
253
254
255
256
930227

Figure A-2.

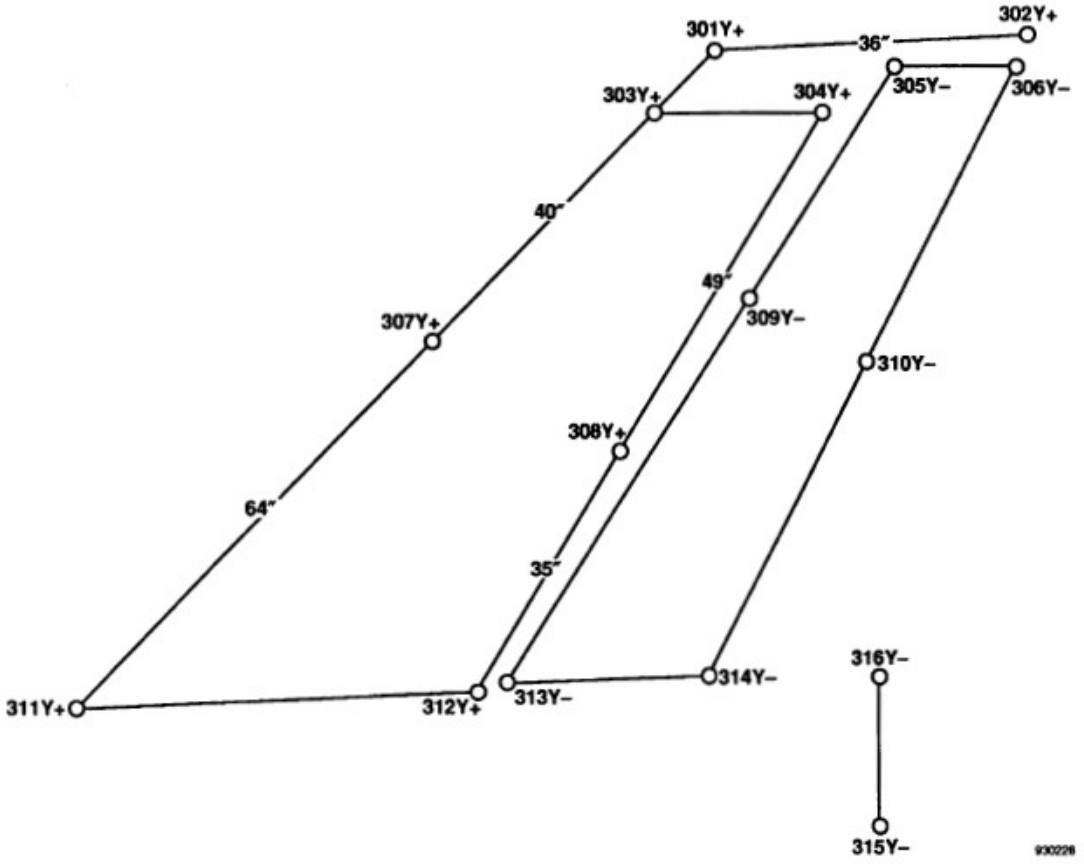
301Y+
302Y+
36"
303Y+
304Y+
305Y–
306Y–
40"
49"
307Y+
309Y–
310Y–
308Y+
64"
35"
316Y–
311Y+
312Y+
313Y–
314Y–
315Y–
930226

Figure A-3.

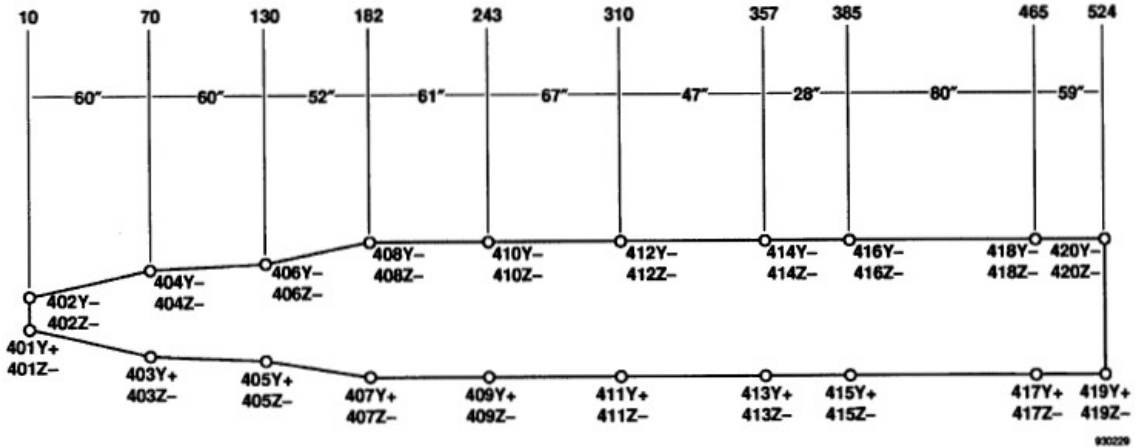
10
70
130
182
243
310
357
385
465
524
60"
60"
52"
61"
67"
47"
28"
80"
59"
401Y+
401Z–
402Y–
402Z–
403Y+
403Z–
404Y–
404Z–
405Y+
405Z–
406Y–
406Z–
407Y+
407Z–
408Y–
408Z–
409Y+
409Z–
410Y–
410Z–
411Y+
411Z–
412Y–
412Z–
413Y+
413Z–
414Y–
414Z–
415Y+
415Z–
416Y–
416Z–
417Y+
417Z–
418Y–
418Z–
419Y+
419Z–
420Y–
420Z–
930229

Figure A-4.